ELSEVIER

Chemical Geology 210 (2004) 201–224

CHEMICAL GEOLOGY
INCLUDING
ISOTOPE GEOSCIENCE

www.elsevier.com/locate/chemgeo

# Fluid evolution in the W–Cu–Zn–Pb San Cristobal vein, Peru: fluid inclusion and stable isotope evidence

S. Beuchat[a,*], R. Moritz[a], T. Pettke[b]

[a] *Section des Sciences de la Terre, University of Geneva, 1205 Geneva, Switzerland*
[b] *Institute for Isotope Geochemistry and Mineral Resources, Federal Institute of Technology ETH, 8092 Zürich, Switzerland*

**Abstract**

The Zn–Pb ± Ag ± Cu San Cristobal district is located 100 km east of Lima in the western cordillera of Peru. It is centred around the Chumpe intrusion and is composed of vein and carbonate replacement ore types. The main San Cristobal vein presents a paragenesis that can be divided into three stages: (a) an early wolframite–quartz–pyrite stage, (b) a quartz–base metal stage, and (c) a late quartz–carbonate–barite stage.

Fluid inclusions in quartz from the tungsten stage are biphase (LV) at room temperature and homogenise to the liquid phase between 146 and 257 °C. Their salinities range between 2.1 and 5.1 wt.% NaCl equiv. Rare inclusions contain an additional crystal of halite and have salinities of 46–54 wt.% NaCl equiv. Data of the first two stages show a decrease in homogenisation temperatures concomitant with a salinity decline. Fluid inclusions in quartz from the late stage homogenise at higher temperatures, between 252 and 323 °C, with salinities ranging between 4.6 and 6.7 wt.% NaCl equiv.

Hydrogen and oxygen isotope data indicate a two-stage evolution. Isotopic compositions of the fluid associated with the first two stages define a trend with constant $\delta^{18}O$ values and decreasing $\delta D$ values ($\delta^{18}O = 3.2‰$ to 5.0‰ V-SMOW and $\delta D = -60‰$ to $-112‰$ V-SMOW), which is interpreted as mixing of a dominantly magmatic component with minor meteoric water that had equilibrated with the host rocks. This interpretation is supported by sulphur and lead isotopic data from previous studies. By contrast, the quartz–carbonate–barite stage bears isotopic characteristics defining a trend with a coupled decrease of $\delta^{18}O$ and $\delta D$ ($\delta^{18}O = -8.1‰$ to 2.5‰ V-SMOW and $\delta D = -57‰$ to $-91‰$ V-SMOW) and is explained by addition of meteoric water to the system and subsequent mixing with a less important magmatic component.

Different fluid origins are confirmed by laser ablation ICP-MS analyses of the triphase (LVH) and biphase (LV) primary inclusions. The concentrations of the major ore elements, i.e., W, Cu, Zn and Pb, decrease throughout the paragenesis; W, and to a lesser extent Cu, show significant variations, associated with a steep decrease in their concentration. The decreasing concentrations can be explained by mineral deposition and dilution by the meteoric fluid; differences in the rate of decrease indicate selective precipitation of W. Fluid inclusions of the quartz–carbonate stages show an abrupt increase in Ba and Sr concentrations. This is interpreted to reflect a higher volume of host rock silicate alteration, probably due to the increasing size of the fluid flow cell and is explained by the input of a third fluid of unknown origin. LA-ICP-MS analyses show that the fluids were already depleted in W and Cu before reaching the emplacement of carbonate replacement ore type, whereas Zn and Pb were still present in considerable amounts. This is

* Corresponding author. Tel.: +41-22-379-66-26; fax: +41-22-379-32-10.
*E-mail address:* Sebastien.Beuchat@terre.unige.ch (S. Beuchat).

0009-2541/$ - see front matter © 2004 Elsevier B.V. All rights reserved.
doi:10.1016/j.chemgeo.2004.06.008

again due to selective precipitation and is consistent with the interpretation that the economically interesting metals were dominantly introduced by magmatic fluids.
© 2004 Elsevier B.V. All rights reserved.

*Keywords:* Fluid inclusion; Stable isotope; Laser ablation; Ore deposit; Hydrothermal fluid

## 1. Introduction

Vein and carbonate replacement Zn–Pb–Cu–Ag deposits are common ore types of the Miocene metallogenic belt of central and northern Peru (Noble and McKee, 1999) and include some world-class districts such as Cerro de Pasco, Colquijirca, Morococha and San Cristobal. Even though some writers have interpreted some of these carbonate replacement ores to be diagenetic in origin (Dalheimer, 1990; Kobe, 1990a), field relations and lead isotope systematic strongly argue in favour of an epigenetic origin related to Miocene magmatism (Moritz et al., 2001; Beuchat, 2003). The genetic interpretations, and especially the sources of fluid and the mechanisms of ore deposition, have been the subject of many studies and different interpretations. For instance, Rye and Sawkins (1974) at Casapalca, Deen et al. (1994) at Julcani and Heinrich (1990) at San Cristobal have found strong stable isotopic evidences for the presence of a magmatic fluid component and for mixing with meteoric water. An alternative interpretation was suggested by Campbell et al. (1984) who interpreted the San Cristobal data as "a meteoric fluid which has experienced exchange at very low water to rock ratios ($<0.05$)". Based on elemental and stable isotope chemistry, Landis and Rye (1974) and Norman and Landis (1983), at Pasta Bueno, have argued that a significant connate component was added to the meteoric and magmatic fluids. Similarly, lead and sulphur isotope data suggest that, in some deposits, some elements were derived from sources other than the adjacent magmatic rocks. Such contrasting interpretations about the sources of fluid and the depositional mechanisms are not only characteristic of the Miocene metallogenic belt of central and northern Peru, but are common features of such ore deposits worldwide. Indeed, the genetic interpretation of similar ore deposits in the Western United States and Mexico have led to a similar debate (Megaw et al., 1988, 1996; Beaty et al., 1990; Smith, 1996; Titley, 1996).

Here, we focus on a single vein of the San Cristobal district in which the paragenetic sequence is well established (Stucky, 2001; Lisboa, 2002; Beuchat, 2003) to trace the different fluid sources and mechanisms of ore deposition from the beginning to the end of the mineralising system. We present new detailed microthermometric, Raman spectroscopic and LA-ICP-MS fluid inclusion data, along with new stable isotopic results that complement those obtained by Campbell et al. (1984). Integration with previous Sr, Pb and S isotopic data (Moritz et al., 2001) permits tracing of the mineralising process from the fluid exsolved from the magma to the quartz–carbonate stages of ore deposition. Such a detailed study reveals a much more complex evolution than expected, with at least three different fluids and multiple physicochemical processes such as fluid mixing, fluid/rock interaction, $CO_2$ degassing and heterogeneous fluids with halite crystals trapping. This study shows that, while fluids from different origins affected the entire area, base metals in that district were most likely provided by a magmatic fluid.

## 2. Regional geological setting

The San Cristobal district is located 110 km east of Lima in the western cordillera of Peru (Fig. 1). It is mainly composed of Paleozoic phyllites of the Excelsior Group, Permo-Triassic volcaniclastic rocks of the Mitu Group, Triassic–Jurassic carbonate rocks of the Pucará Group, Cretaceous sedimentary rocks and Miocene intrusions (Fig. 1). The Excelsior Group is the oldest rock unit exposed in the district and it crops out in the core of the Chumpe Anticline (Fig. 1). This is a heterogeneous unit that includes shales, phyllites, limestones, quartzites and basaltic flows where pillow lavas can be recognised in places (Kobe, 1990b). A

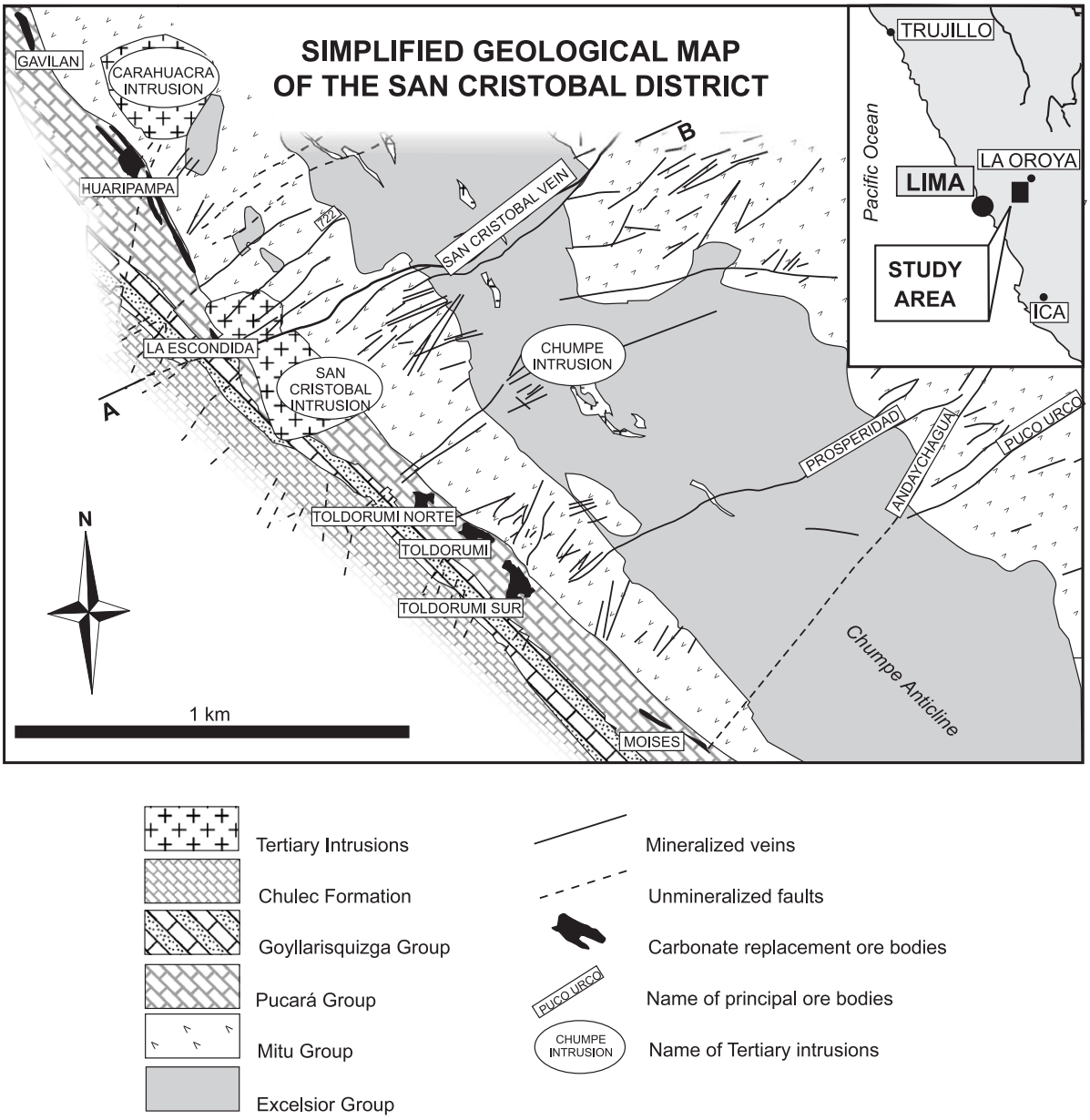


Fig. 1. Location and simplified geology of the San Cristobal district, and location of the vein systems and principal ore bodies.

distinct angular unconformity exists between the Excelsior phyllites and the overlying Mitu volcaniclastic rocks. The Triassic–Jurassic carbonates of the Pucará Group rest unconformably on the Mitu Group and are intensively brecciated at their base. The Pucará Group is overlain by different sedimentary Cretaceous units, including the Goyllarisquizga Group and the Chulec Formation (Fig. 1).

Igneous rocks of Tertiary age are well exposed in the Domo de Yauli area and are best represented in the Morococha district (Beuchat, 2003). At San Cristobal, three different intrusions have been recognised: the

Carahuacra, San Cristobal and Chumpe intrusions (Fig. 1). Geochronological and structural data indicate that the ore deposits are temporally related to the youngest Chumpe intrusion, dated at 6.6 (+1/−3.6) Ma by U/Pb dating of zircons (Beuchat et al., 2001; Beuchat, 2003). It consists of a series of small plugs and dykes of felsic composition intruded along the axis of the Chumpe anticline (Fig. 1). The width of these dykes ranges from several decimetres to tens of metres. The primary mineralogy is obscured by intense alteration. Primary minerals include quartz eyes and highly altered phenocrysts of plagioclase and K-feldspar, set in an aphanitic groundmass consisting predominantly of quartz, sericite, kaolinite, illite, pyrite and alunite (Beuchat, 2003). The least altered samples are characterised by chlorite and epidote alteration. In such samples, relics of biotite and some amphiboles can be recognised. Quartz eyes of the Chumpe intrusion contain crystallised melt inclusions; their crystallisation may have occurred from reopening and introduction of later fluids because they are generally crosscut by trails of secondary fluid inclusions (Halter et al., 2002). These secondary fluid inclusions are highly variable in shape, but round and negative crystal forms are the most prevalent (Bartlett, 1984). The majority are either vapour-rich (L/V>80%) or contain solids optically recognised as halite and/or sylvite crystals. Measured fluid inclusion homogenisation temperatures (LV → L and LV → V) range between 305 and 434 °C and salinities cover the whole range between 2.7 and 49.0 wt.% NaCl equiv., most being between 10 and 30 wt.% NaCl equiv. (Bartlett, 1984).

Two ore deposit types are recognised in the San Cristobal district: Zn–Pb ± Ag ± Cu veins and Zn–Pb ± Ag carbonate replacement bodies. Nearly all major faults present in the San Cristobal district and crosscutting the Domo de Yauli structure are mineralised to some extent and the larger ones are presently exploited for Zn, Pb, Cu and Ag. Whereas faults crosscut rocks of all lithologies (Figs. 1 and 2), the vein ore type is restricted to the Excelsior phyllites, Mitu volcanic rocks and Tertiary intrusions. The vein system is composed of a series of subparallel veins and the San Cristobal vein is the major vein of the district (Figs. 1 and 2). Zn–Pb ± Ag carbonate replacement deposits are hosted by carbonate rocks of the Pucará Group and occur along the contact with the underlying Mitu Group; their position coincides with the location where veins extend from the Mitu rocks

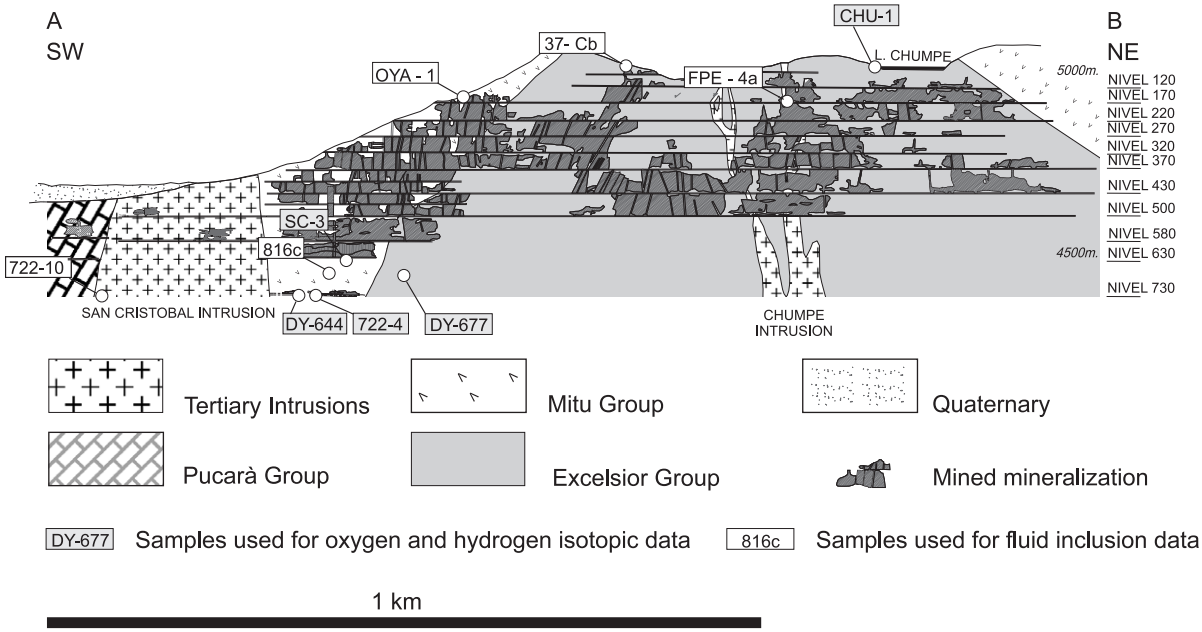


Fig. 2. Schematic longitudinal section of the San Cristobal vein with location of samples. Location of the cross section on Fig. 1.

into the Pucará limestones (Fig. 1; Bartlett, 1984; Beuchat, 2003).

Although studies on specific veins reveal small discrepancies, such as the presence of the early wolframite stage or accessory Ag-bearing phases, the paragenetic sequence of the San Cristobal vein is representative of the district (Campbell et al., 1984; Stucky, 2001; Lisboa, 2002; Beuchat, 2003). Detailed investigations of hand specimens and polished and thin sections indicate a depositional sequence that can be subdivided into three main stages. The early *wolframite–quartz–pyrite stage* is characterised by tabular crystals of wolframite and euhedral crystals of pyrite, generally enclosed in quartz (Fig. 3a). The quartz is milky and shows undulous extinction in thin section. Only crystals in pressure shadows of pyrite and/or wolframite show no sign of deformation. Trace amounts of sericite and augelite

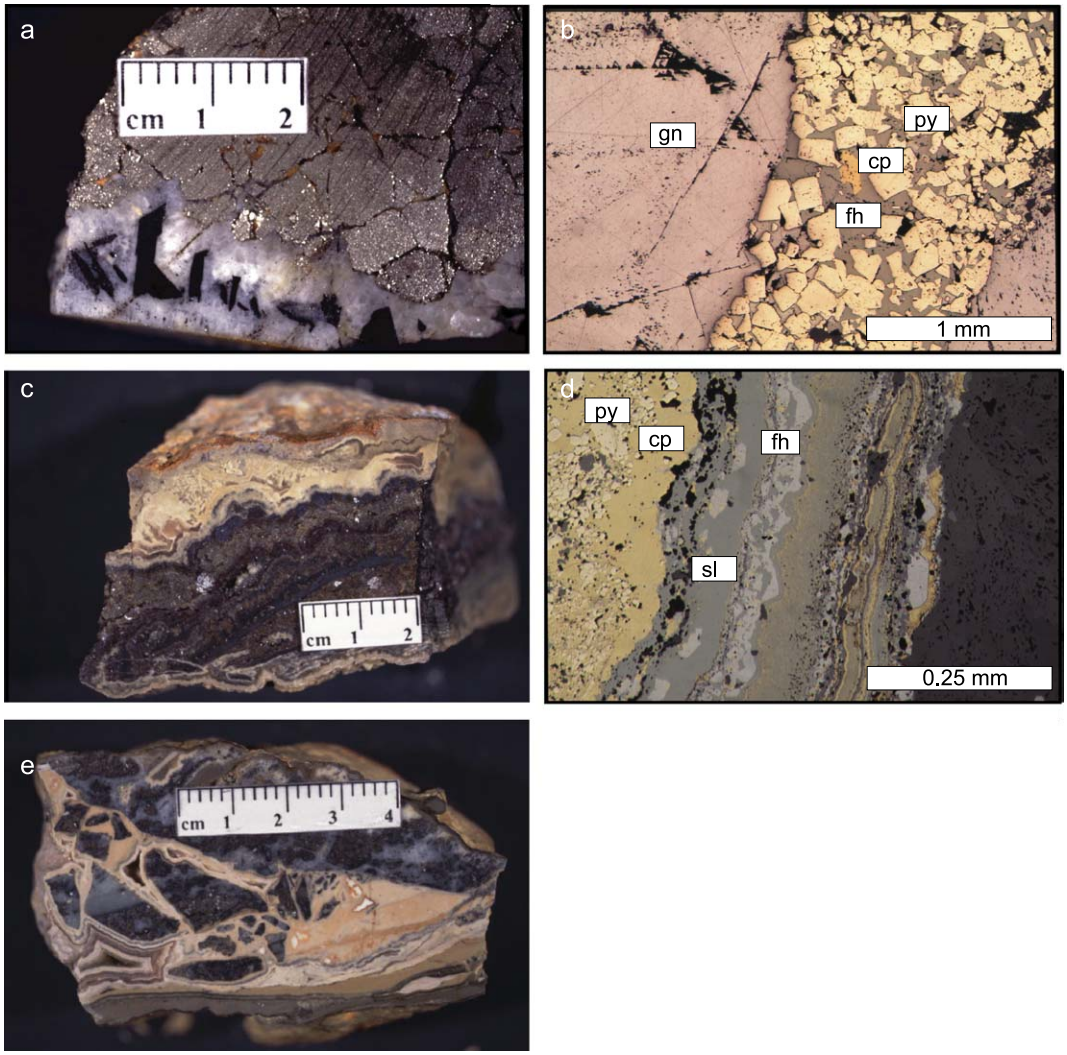


Fig. 3. Ore sample of the veins. (a) Tungsten stage showing vein of quartz and wolframite crosscutting massive pyrite. (b) Breccia texture on a small scale showing brecciation events during the time of the base metal stage. (c, d) Typical concretion texture on two different scales indicating repetitive mineral deposition. (e) Breccia texture with clasts of the base metal stage consisting of sphalerite, galena and quartz, set in a matrix of carbonate and trace amount of barite. py: pyrite, gn: galena, sl: sphalerite, fh: fahlore.

can be observed in places (Campbell et al., 1984). The distribution of this tungsten stage is directly linked to the proximity to the Chumpe intrusion (Pastor, 1970). For example, tungsten ore is absent in veins that do not crosscut the Chumpe intrusion. The *quartz–base metal stage* is volumetrically by far the most important and is dominated by pyrite, sphalerite, chalcopyrite, galena and quartz (Fig. 3b–e). Accessory minerals include marcasite, pyrrhotite, arsenopyrite, freibergite, boulangerite, allabandite, bismuthinite, argentite, pyrargirite and stannite (Stucky, 2001; Lisboa, 2002). Brecciation and concretion textures are common (Fig. 3b–e). During the year 2001, ore grades were around 7.32 wt.% Zn, 1.18 wt.% Pb, 0.34 wt.% Cu and 3.83 oz/t Ag for a production of 836,000 metric tons (Volcan compañia minera annual report, 2001). These ore grades are highly variable because the ore minerals are not equally distributed. For example, Cu ore is highly enriched at the contact between the volcanic rocks of the Mitu Group and the Excelsior phyllites. The late *quartz–carbonate–barite stage* is mainly composed of carbonates such as rhodochrosite, Mn-rich siderite and ankerite and associated with the deposition of large crystals of euhedral quartz and carbonates (Fig. 3b and d). The carbonates crystallised in vugs and developed rhombohedral crystals (close to the contact between volcaniclastic rocks and limestones). In some cases, barite was deposited after the carbonates. In other locations, the carbonates form colloform textures and, instead of barite, small pockets of dickite are present. Finally, silicified, platy calcite crystals have been found at the surface and are evidence for boiling during the late quartz–carbonate–barite stage (Simmons and Christenson, 1994; Simmons et al., 2000).

Hydrothermal alteration of the volcanic rocks of the Mitu Group and the Miocene intrusions adjacent to the veins is of two successive types, defined as sericite–argillic and chloritic. The sericite–argillic alteration is recognised in a vein halo of a few meters and results in the conversion of primary plagioclase, biotite and amphibole to sericite, kaolinite and dickite. Sericite has been dated with the $^{40}Ar/^{39}Ar$ method by Beuchat et al. (2001) at $4.78 \pm 0.16$ Ma. This zone is also correlated with the pervasive development of pyrite. As already noted by Pastor (1970), the volume of the sericite–argillic alteration decreases west from the Chumpe intrusion. The chloritic alteration halo is up to tens of meters wide and characterised by the development of chlorite and carbonate. These two alteration zones are less developed in phyllites and may even be totally absent. Additionally, strong silicification can occur in phyllites.

## 3. Analytical methods

For the microthermometric fluid inclusion study, 100-μm-thick doubly polished wafers were prepared for quartz samples. Measurements were performed on a Linkam THMSG-600 heating–freezing stage mounted on a DMLB Leica microscope equipped with a Nikon 100× long working distance lens. The system was calibrated with synthetic fluid inclusions at −56.6, 0.0 and 374.1 °C (Sterner and Bodnar, 1984). Low-temperature measurements have an uncertainty of ±0.1 °C, whereas high-temperature measurements have a precision of ±1 °C. Salinities were calculated in the $NaCl–H_2O$ system from the final ice melting temperature for biphase (LV) inclusions, using equations published in Bodnar and Vytik (1994). In the case of triphase (LVH) inclusions, salinities were calculated either by halite dissolution (Sterner et al., 1988) or using volume ratios (Sheperd et al., 1985), the latter being used for cases where fluid inclusions decrepitated before the final dissolution of halite. As pointed out by Hedenquist and Henley (1985), salinity estimates based on final ice melting measurements are frequently biased by the presence of volatile solutes such as $CO_2$. The amount of $CO_2$ dissolved in the fluid inclusions of this study is very low and variable, but certainly leads us to small errors in the estimated sodium chloride content. If Raman spectrometry allowed us to detect $CO_2$ in the largest inclusions, it did not allow to analyse the $CO_2$ content of the smallest inclusions (i.e., <12 μm; Beuchat, 2003). Corrections could therefore be only applied to the latter, and add an additional factor of uncertainty, due to the different sizes of the fluid inclusions.

The $CO_2$ content of the fluid inclusions was determined with Raman spectroscopy using the method of Rosso and Bodnar (1995). Our measurements were performed on a Labram Raman microprobe with a modified Olympus microscope. Raman spectra were

recorded using the 534-nm line from a Coherrent DPSS 534 Nd-YAG laser.

The LA-ICP-MS consists of an Elan 6000 ICP-MS instrument (Perkin-Elmer) combined with a 193-nm excimer laser (Compex 110 I, ArF, Lambda Physics; Günther and Heinrich, 1999; Pettke et al., 2000). Fluid inclusions used in this study tended to decrepitate during analysis, as one tried to directly ablate them with a large beam size. This was avoided by opening the inclusion with a pit much smaller than the inclusion and then by increasing the size of the pit in several steps as soon as the first signal appeared. It allowed us to improve reproducibility for elements that are present in daughter crystals (Günther et al., 1998). Pits of 4, 10, 20, 40 and 60 μm in diameter were used. The resulting signals were integrated and compared to signal intensities from reference material (NBS 610 glass from NIST), allowing calculation of relative elemental abundances in the inclusion (Longerich et al., 1996). The elemental ratios were transformed into absolute concentration by using an internal standard with the aid of the equivalent salinity determined by microthermometry. The NaCl equivalent value was corrected for other major cations present in the inclusion (K, Fe and Mg) according to Heinrich et al. (1992). In fluids that are dominated by Na, the uncertainty associated with this correction is estimated to be around 10–20 relative percent (Heinrich et al., 2003).

Hydrogen and oxygen isotope analyses were performed on minerals and fluid inclusions at Queen's University, Kingston, Canada. Sphalerite samples used for stable isotope analysis of fluid inclusions were carefully selected to avoid secondary fluid inclusion trails as much as possible. The values are reported as per mil deviations relative to the V-SMOW standard. Errors reported are ± 0.2‰ for oxygen in minerals and ± 2‰ in fluid inclusions. The error for hydrogen is ± 5‰.

## 4. Fluid inclusion petrography, microthermometry and Raman spectroscopy

The paragenesis of the San Cristobal vein indicates three successive quartz generations that host fluid inclusions. They are related to the three different stages of mineralisation described above; quartz I is associated with the early wolframite–quartz–pyrite stage, quartz II with the quartz–base metal stage and quartz III with the quartz–carbonate–barite stage. Table 1 gives an overview of the fluid inclusion characteristics.

Quartz I is generally milky and contains a series of dotted black lines interpreted as decrepitated fluid inclusions trapped along the growth zones (Fig. 4, Type $A_{\mathbf{I}}$). Only a few inclusions have preserved their original fluid content, but as they are connected by thin tubes and have variable phase ratios at room temperature, they are probably necked down and were therefore not analysed. Intact fluid inclusions could only be found within pressure shadows of wolframite and pyrite crystals. In such zones, four different types of $H_2O$–NaCl–(KCl) inclusions can be recognised (Fig. 4, Table 1):

*Type $A_{II}$* are triphase (LVH) rounded inclusions with a diameter between 7 and 15 μm. They form isolated, small clusters of a few inclusions within grains, never form trails and their host quartz is free of secondary inclusions; they are possibly primary in origin. Homogenisation temperatures (LVH → LH) range between 206 and 259 °C and the salinity varies from 46.1 to 54.0 wt.% NaCl equiv. The final dissolution temperature of halite was obtained for only one inclusion before decrepitation (Appendix A, inclusion no. 3 at 436 °C). To preserve some inclusions for LA-ICP-MS analyses, salinities were determined on the basis of phase ratios in two cases (Appendix B, inclusions no. 1 and 2). Carbon dioxide was not detected in the triphase (LVH) inclusions using Raman spectrometry.

*Type $A_{III}$* inclusions are slightly larger and occur in a similar location as type $A_{II}$ inclusions, but they are biphase (LV) and have a more angular morphology (Fig. 4). They may also be interpreted as primary fluid inclusions. Their homogenisation temperatures cover a large range of temperature (146–239 °C) and salinities vary from 2.9 to 5.1 wt.% NaCl equiv. Homogenisation and ice melting temperatures are consistent within the same cluster of inclusions. $CO_2$ was detected by Raman spectroscopy in one, 20-μm inclusion (inclusion 17, $CO_2$ density of 0.6 g/cm$^3$), but the majority of the Raman analyses did not reveal any $CO_2$ bands.

Table 1
Summary table of the fluid inclusions of this study, including their descriptive properties, microthermometry and $CO_2$ content determined by Raman spectroscopy

| Stages | Number of phases at room temperature | Location and terminology[a] | Morphology | Size (μm) | *N* | Salinity (wt.% NaCl equiv.) | Homogenisation $T^b$(° C) | $CO_2$ (g/cm$^3$) |
|---|---|---|---|---|---|---|---|---|
| *Early wolframite–pyrite–quartz I stage, sample FPE-4a* | | | | | | | | |
| AII | 3-LVH | clusters of few inclusions within grains; primary | rounded | 7–15 | 3 | 46.1–54.0 | 436 | – |
| AIII | 2-LV | clusters of few inclusions within grains; primary | rounded | 8–30 | 15 | 2.9–5.1 | 146–239 | 0–0.6 |
| AIV | 2-LV | along trails cutting grain edges; secondary | irregular | 8–50 | 24 | 2.1–5.1 | 155–257 | 0–0.5 |
| *Quartz II–base–metal stage, samples DY-37C, 816c, OYA-1* | | | | | | | | |
| BI | 2-LV | along trail within grains; pseudosecondary | thin and tabular | 8–15 | 3 | 3.9–4.0 | 328–337 | 0–0.3 |
| BII | 2-LV | along trails cutting grain edges; secondary | elongated, irregular | 5–20 | 8 | 2.7–4.2 | 155–240 | – |
| *Late quartz III–carbonate–barite stage, sample 722-10* | | | | | | | | |
| CI | 2-LV | along growth zone; primary | elongated | 15–30 | 6 | 5.9–6.7 | 302–323 | 0–0.4 |
| CII | 2-LV | small cluster within grains; primary | rounded | 20–60 | 3 | 5.4–6.2 | 263–275 | – |
| CIII | 2-LV | along crosscutting ribbon; secondary | irregular | 15–50 | 10 | 4.6–6.2 | 253–319 | 0–0.4 |

*N* = number of fluid inclusion measurements.
[a] Terminology according to Roedder, 1984.
[b] All inclusions homogenize to the liquid phase.

*Type $A_{IV}$* inclusions are by far the most abundant. They are biphase (LV) and clearly secondary because they form large ribbons crosscutting grain boundaries. They are very irregular and their size is generally larger, from 8 to 50 μm, than the previous types (Fig. 4). Homogenisation temperatures vary from 155 to 257 °C, and salinities are between 2.1 and 5.1 wt.% NaCl equiv. Raman spectra of type $A_{IV}$ inclusions indicate variable amounts of $CO_2$ with a density below 0.5 g/cm$^3$; no $CO_2$ was detected into the smallest inclusions, below 15 μm in diameter.

Finally *type $A_V$* inclusions consist of numerous trails of biphase (LV) fluid inclusions that crosscut all other inclusion assemblages. These were not analysed due to their very small size, which is less than a few microns.

The wolframite- and quartz-hosted fluid inclusions of this early vein stage have previously been studied by Campbell and Robinson-Cook (1987). As discussed below, their data on quartz and wolframite from the tungsten stage indicate similar salinities but higher homogenisation temperatures than those measured in this study (Fig. 5).

The base metal stage is accompanied by abundant quartz II deposition. Probably due to the successive brecciation events, this quartz is milky and intensely fractured with the consequence that few inclusions survived and none are unequivocally primary. The few preserved inclusions can be divided into two types of biphase (LV), $H_2O$–NaCl–(KCl) inclusions (Table 1). Except for one inclusion, no $CO_2$ was detected. This may be due either to its absence, or to the small size of these inclusions, as observed for type $A_{IV}$ inclusions:

*Type $B_I$* corresponds to thin tubular inclusions with a maximum length of 15 μm. They form trails but do not crosscut grain edges. Their shapes make microthermometric measurements difficult. A few inclusions yielded homogenisation temperatures

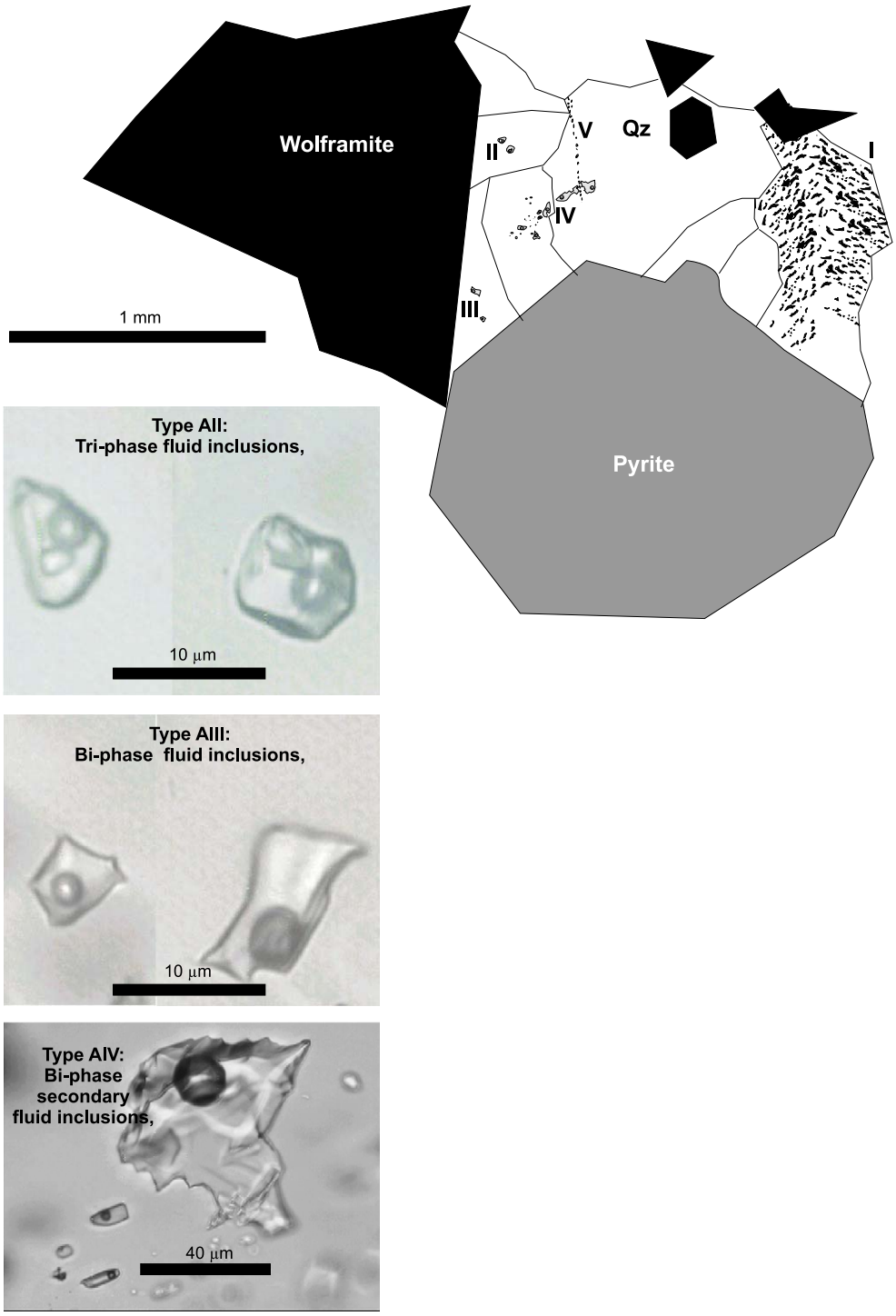


Fig. 4. Petrography of the early vein stage representing the five types of fluid inclusions present in quartz I. Typical large inclusions of type $A_{II}$, $A_{III}$ and $A_{IV}$ are represented by photomicrograph. Inclusions are not to scale.

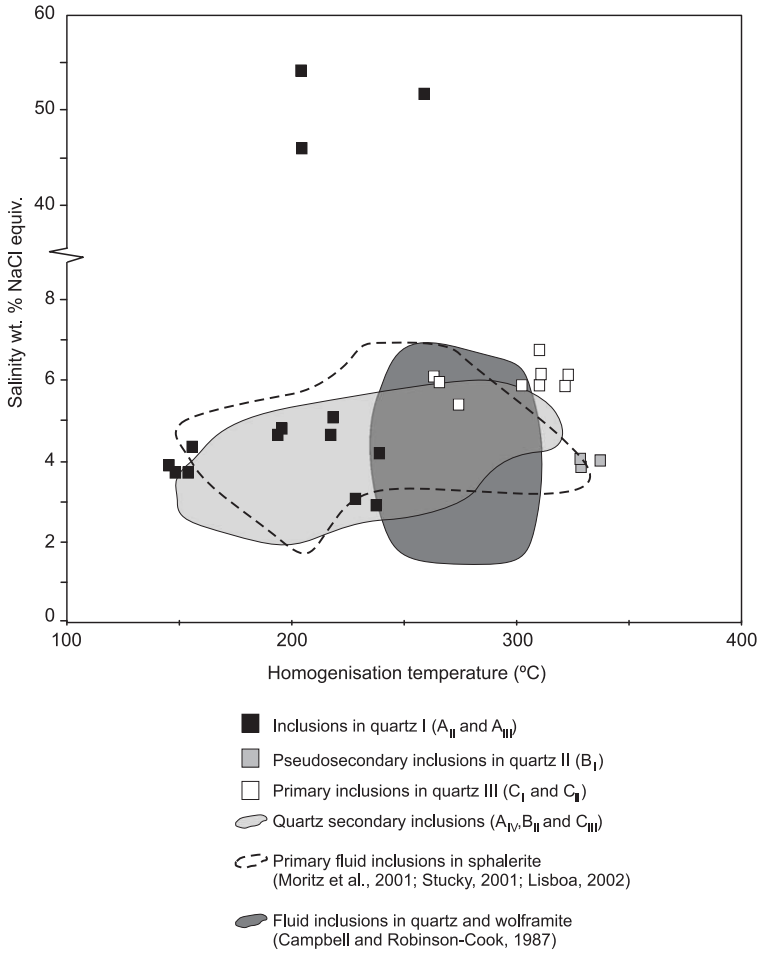


Fig. 5. Salinity vs. homogenisation temperature of fluid inclusions determined by microthermometric measurements. Salinities are calculated with equations of Bodnar and Vytik (1994).

between 328 and 337 °C and salinities of around 4 wt.% NaCl equiv.

*Type $B_{II}$* inclusions are numerous, secondary and are found in each of the base-metal stage samples. They have a size between 5 and 20 μm and in some samples where they are elongated, as with type $B_I$, they are more irregular in shape. Type $B_{II}$ inclusions were only analysed in samples containing the largest inclusions. Homogenisation temperatures cover the whole range between 155 and 240 °C and salinities from 2.7 to 4.2 wt.% NaCl equiv.

A large number of fluid inclusion analyses exists for sphalerite associated with quartz II deposition, where criteria for primary origin are easier to determine (Campbell et al., 1984; Stucky, 2001; Lisboa, 2002; Moritz et al., 2001). Whereas primary inclusions in sphalerite cover more or less the same range of temperatures as secondary inclusions in quartz II, their salinity appears to be slightly higher (Fig. 5). The quartz-hosted secondary inclusions probably post-date ore deposition.

The latest stage of the vein paragenesis consists of quartz III, Mn-rich siderite, rhodochrosite, ankerite and barite. Unlike quartz I and II, quartz III is euhedral and very clear, permitting reliable distinction among different types of inclusions (Fig. 6, Table 1). All inclusions of this stage are biphase (LV) and

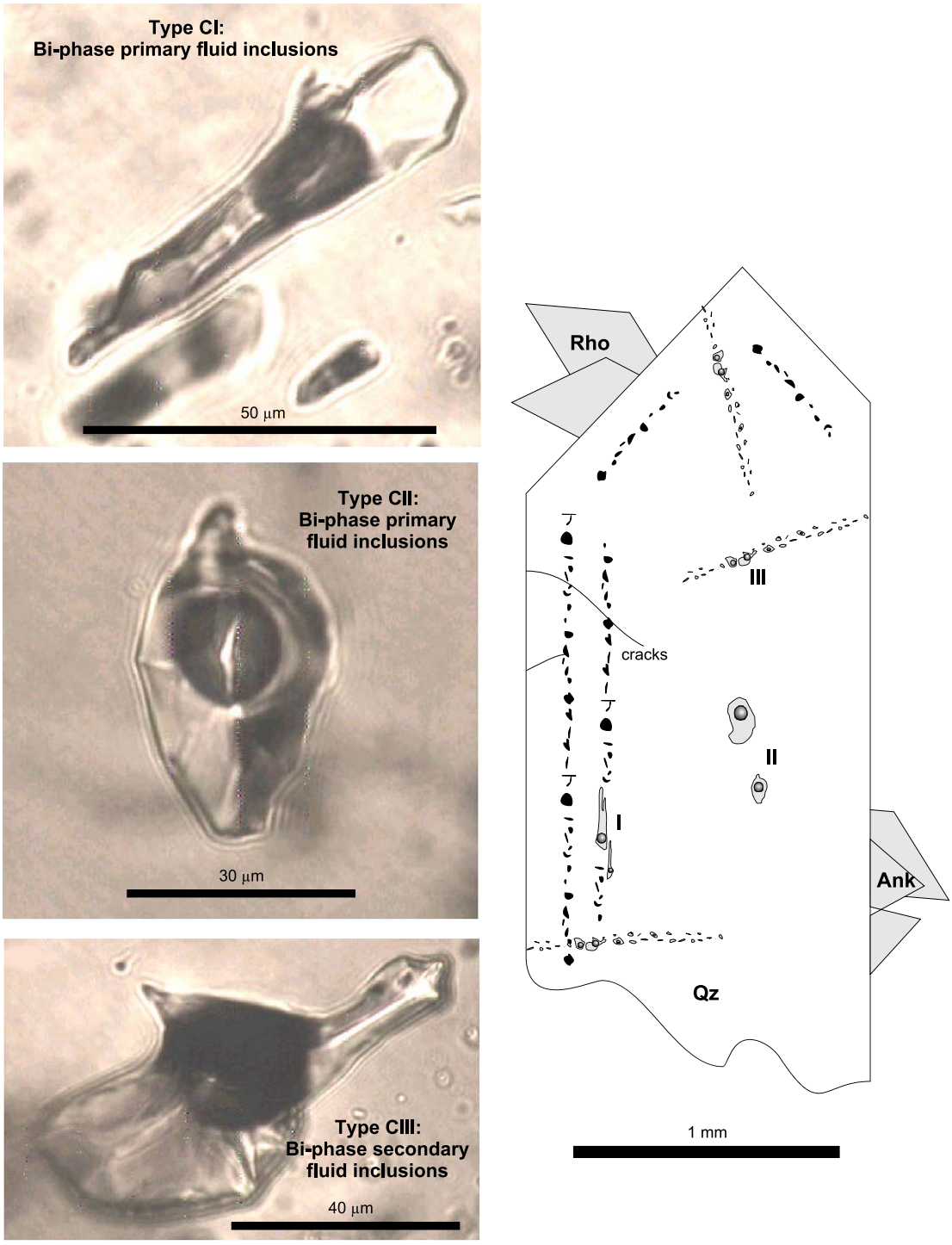


Fig. 6. Petrography of the late vein stage representing the three different types of inclusions. Largest inclusions of each types are shown on photomicrograph. Inclusions are not to scale. Qz: quartz, Rho: rhodochrosite, Ank: ankerite.

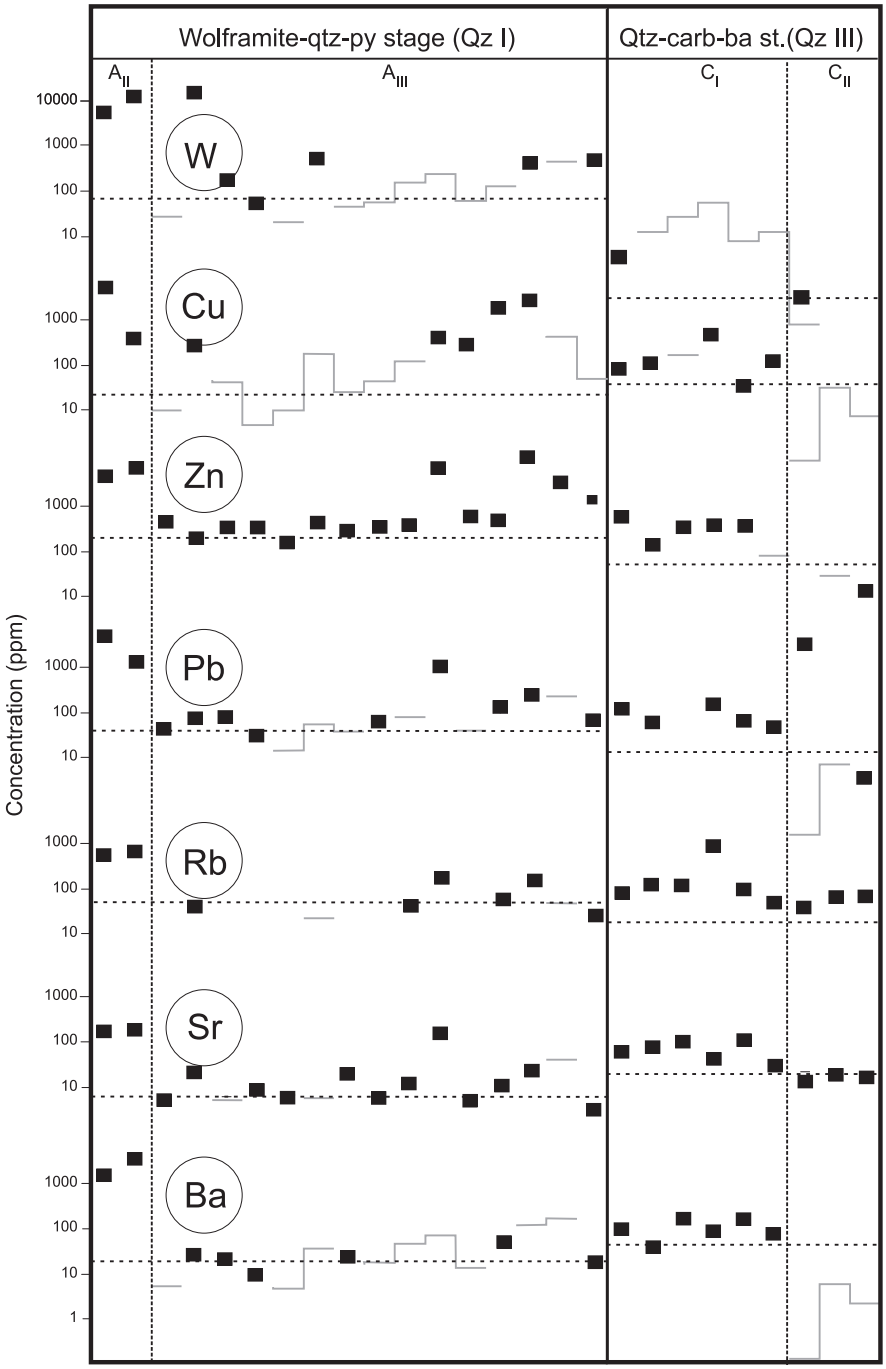


Fig. 7. Evolution of the fluid W, Cu, Zn, Pb, Rb, Sr and Ba concentrations reconstructed from LA-ICP-MS analysis and microthermometric study of inclusions of the wolframite–quartz–pyrite and the quartz–carbonate–barite stages. Plain grey lines represent LOD where concentration is below. Dotted lines represent the mean value of secondary fluid inclusions of each stage. Inclusions are sorted according to interpreted petrographic timing and decreasing homogenisation temperature. Concentrations are given in ppm.

composed of $H_2O$–NaCl–(KCl) fluids. Unlike the other fluid inclusion families, they contain commonly variable amounts of dissolved $CO_2$ with a density up to 0.5 g/cm$^3$:

*Type $C_I$* consists of large elongated inclusions (up to 30 μm) along primary growth zones (Fig. 6). Some of the inclusions located in these growth zones appear to be decrepitated. Careful observations reveal that these decrepitated inclusions are located in zones with abundant very fine cracks. However, parts of the growth zone are far from such zones and fluid inclusions are preserved in these areas. Furthermore, homogenisation temperatures and salinities are within a narrow range, from 302 to 323 °C and from 5.9 to 6.7 wt.% NaCl equiv., respectively (Table 1).

*Type $C_{II}$* consists of three large, rounded fluid inclusions located at the centre of a crystal (Fig. 6). They are isolated, far away from secondary inclusion trails and growth zones, and are interpreted to be primary. Their homogenisation temperatures range from 263 to 275 °C and salinities vary between 5.4 and 6.2 wt.% NaCl equiv. (Table 1).

*Type $C_{III}$* inclusions are located along trails that start at the crystal border (Fig. 6) and are therefore secondary in origin. They homogenise between 253 and 319 °C and have salinities ranging from 4.6 to 6.2 wt.% NaCl equiv. (Table 1).

Inclusions in quartz III apparently yield variable data. Lisboa (2002) reports primary inclusions in quartz III that homogenise between 150 and 246 °C, with salinities ranging from 2.4 to 4.5 wt.% NaCl equiv. Whereas no fluid inclusions of sufficient size have been found in the associated carbonates, barite crystals contain large inclusions (up to tens of microns) that homogenise between 136 and 159 °C and have salinities ranging from 1.6 to 3.5 wt.% NaCl equiv. (Lisboa, 2002). However, none of these inclusions is considered primary in origin.

## 5. Fluid inclusion LA-ICP-MS results

$A_{II-IV}$, $B_{II}$, $C_{I-III}$ inclusion types were analysed for Na, K, Fe, Cu, Zn, Sr, Ag, Sn, Ba, W and Pb, whereas Mg, Ca, Mn, As, Rb, Y, Mo and Ce were determined only for a minority of fluid inclusions (Appendix A). Yttrium, Mo, Mg, Ca, Ag, Sn and Ce were generally below the limits of detection (LOD) and are therefore not reported in Appendix A (see Beuchat, 2003, for the complete set of analyses). The limits of detection can be high in many cases due to the small size and low salinity of the fluid inclusions. Inclusions with a significant W content are exclusively hosted by quartz I (Fig. 7). On the other hand, distinctive elements of the base metal stage, e.g., Cu, Zn, Pb and As, were detected in all inclusion types; concentrations of these metals decrease through the paragenesis and secondary inclusions have lower concentrations than in primary inclusions of the same sample (Fig. 7). Some elements, such as Ba and Sr, exhibit the reverse behaviour, in that their concentration is higher in inclusions hosted by quartz III relative to those associated with earlier paragenetic stages (Fig. 7). Potassium, Fe, Mn and Rb are elements that were detected in all paragenetic stages and their concentrations do not show any systematic variations between the different quartz stages. Some $A_{III}$ inclusions contain much higher concentrations of elements than other inclusions of the same type (for example, inclusion FPE-4a no21, Appendix A). This may be due to the presence of undetected small trapped solids (see discussion below).

## 6. H and O isotopes

Hydrogen and oxygen isotope analyses (Table 2) were performed to complement the isotopic study of Campbell et al. (1984). The isotopic compositions of fluids measured by Campbell et al. (1984) show a narrow range of $\delta^{18}O$ and very variable $\delta D$ values, which are confirmed by our analyses (Trend A in Fig. 8). Indeed, our wolframite and quartz I samples are within error of the field defined by Campbell et al. (1984). Quartz II has a lower $\delta D$ value, which tends to extend the large range of $\delta D$ values (Fig. 8). Campbell et al. (1984) confirmed these variable $\delta D$ values and the narrow range $\delta^{18}O$ values for fluid inclusions trapped in sulphides minerals. However, hydrogen isotope analyses of fluid inclusions remain difficult to interpret. Although samples of quartz I could be selected to minimise the number of secondary fluid

Table 2
Hydrogen and oxygen isotope compositions

| Sample | Mineral | Ore type | δD (‰ SMOW) | $\delta^{18}$O (‰ SMOW) |
|---|---|---|---|---|
| CHU-1 | Wolframite | Early vein stage | – 97 | 2.8 |
| CHU-1 | Quartz I | Early vein stage | – 107 | 13.8 |
| 722-4 | Quartz II | Base metal vein stage | – 137 | 12.3 |
| DY-677 | Sphalerite | Base metal vein stage | – 79 | |
| DY-644 | Dickite | Late vein stage | – 110 | 9.0 |
| SC-3 | Dickite | Late vein stage | – 101 | 8.7 |

Uncertainties are equal to ± 0.2‰ for $\delta^{18}$O and ± 5‰ for δD.
δD values are obtained on mineral for dickite and on fluid inclusions for wolframite, quartz and sphalerite.

inclusions (Figs. 4 and 6), this was nearly impossible for quartz II, in which secondary inclusions predominate. The δD value from inclusions in quartz II should therefore be considered with care.

Hydrogen isotopic signatures of fluid inclusions in quartz are systematically lower than those of associated sphalerite and wolframite, and this could be due to contributions from structurally bound water within

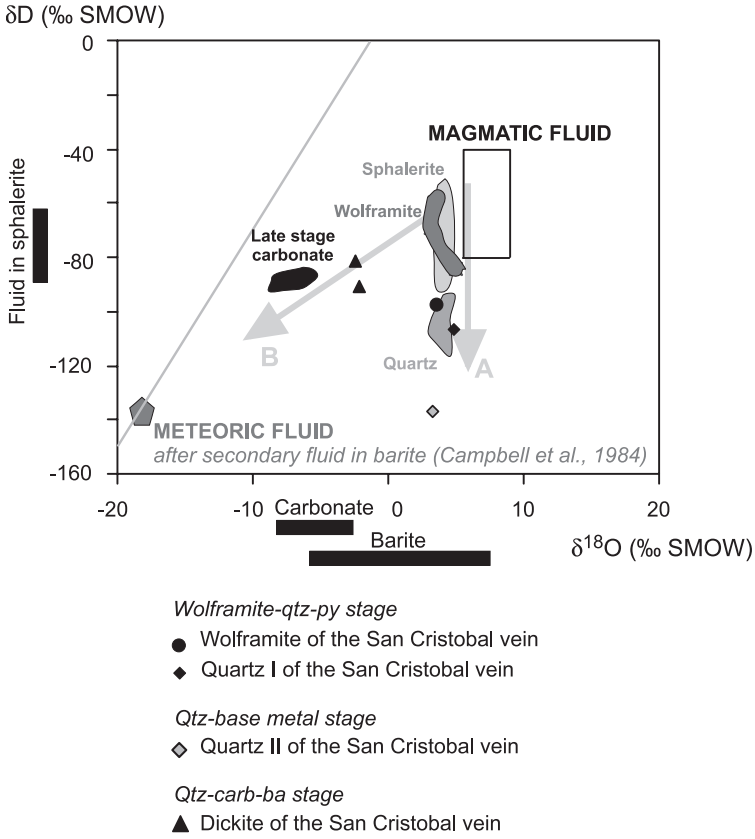


Fig. 8. Hydrogen vs. oxygen isotopic composition of fluids in equilibrium with wolframite, quartz, sphalerite, barite, carbonate and dickite according to fluid inclusion data and equations of Clayton et al. (1972), Kusakabe and Robinson (1977), Land and Dutton (1978), Rosenbaum and Sheppard (1986), Carothers et al. (1988), Zhang et al. (1994) and Gilg and Sheppard (1996). Barite $\delta^{18}$O bar is from Moritz et al. (2001) and carbonate $\delta^{18}$O bar is from Sallier (2002). Grey fields of wolframite, quartz, carbonate and sphalerite and barite δD bar are from Campbell et al. (1984). Field of magmatic water is from Taylor (1974). Trend A represents data of the early vein stage, while trend B represents those of the late vein stage. Modified after Campbell et al. (1984).

quartz (Simon, 2001). Nevertheless, the trend observed for the two tungsten stages remains valid even without the quartz data. The hydrogen isotopic composition of fluid inclusions hosted by the analysed sphalerite is in the same range as those of Campbell et al. (1984). The oxygen isotopic composition could not be determined because the amount of water was too low to permit precise analyses. This is principally due to the selection of a small amount of sphalerite to ensure a predominance of primary inclusions. The isotopic compositions of fluids in equilibrium with late dickite (Fig. 8) are close to the field of paragenetically associated carbonates as defined by Campbell et al. (1984).

## 7. Discussion

### *7.1. Early wolframite–quartz–pyrite and quartz–base metal stages*

The genetic model for the formation of the San Cristobal district has traditionally been explained by a single fluid migrating outward from the Chumpe intrusion. It was suggested to be either a dense magmatic brine that mixed with cooler meteoric water distal to the intrusion (Bartlett, 1984) or a single meteoric fluid that underwent isotopic exchange with a granite at low water to rock ratios (Campbell et al., 1984). A diagenetic model has also been proposed (Dalheimer, 1990; Kobe, 1990a) that has been disputed by several authors (Moritz et al., 2001; Sallier, 2002). All these models were principally based on the morphology of the carbonate replacement ore bodies and the fact that fluid inclusion data indicated only low salinity fluids (< 8 wt.% NaCl equiv.). The only inclusions with higher salinities (up to 49 wt.% NaCl equiv.) reported before this study were secondary inclusions hosted by quartz-eyes in the Chumpe intrusion (Bartlett, 1984). However, this study reveals two different inclusion types in quartz I ($A_{II}$ and $A_{III}$), with similar petrological characteristics but different salinities (Fig. 5). The high salinity of the few primary inclusion types $A_{II}$ recognised in quartz I is evidence for a magmatic fluid component (Bodnar, 1995). Unless the fluid inclusions were modified by postentrapment processes, it is unlikely that the fluid in type $A_{II}$ inclusions was homogeneous at the instant of trapping. Indeed, a homogeneous fluid with halite dissolution temperatures yielding a salinity between 44 and 54 wt.% NaCl equiv. and homogenisation temperatures between 206 and 259 °C implies trapping at a pressure above 3 kbars and a temperature above 400 °C (Sterner et al., 1988; Bodnar and Vytik, 1994). These pressure–temperature conditions are typical for a ductile crustal environment (Fournier, 1999). Such environments are inconsistent with the large open vein structures filled by ore and gangue minerals characteristic of a more shallow, brittle crustal environment. The $A_{II}$ type inclusions are interpreted as forming by accidental trapping of both salt and liquid. The high salinities are probably due to sudden decompression in the fluid exsolved by the magma (Fournier, 1999) and the absence of the steam counterpart in the fluid inclusions of the vein is interpreted as being due to its escape before ore deposition. This is confirmed by the numerous vapour-rich secondary fluid inclusions observed in the Chumpe quartz eyes that homogenise at higher temperatures, between 305 and 434 °C.

Even if $A_{II}$ and $A_{III}$ fluid inclusions share similar petrological features, their relative temporal relationship is unclear because they never occur together. Two alternatives should therefore be considered:

*$A_{II}$ and $A_{III}$ fluid inclusions are contemporaneous*. Based on the model proposed by Fournier (1999), a possible explanation for this alternative is that solids of salt detected in $A_{II}$ inclusions represent the sporadic input of a brine across the brittle–ductile transition from a deep magmatic system into the overlying hydrothermal system dominated by lower salinity fluids represented by $A_{III}$ inclusions.

*$A_{II}$ and $A_{III}$ fluid inclusions are not contemporaneous*. In this case, they represent different stages in the evolution of the hydrothermal system. Because $A_{II}$ fluid inclusions occur only in the early wolframite–quartz–pyrite stage, they could represent the early magmatic-dominated system. On the other hand, $A_{III}$ fluid inclusions have similar microthermometric characteristics as the primary inclusions in the quartz–base metal stage. They may represent the beginning of the dilution indicated by microthermometric fluid inclusion data (Fig. 5). $A_{III}$ and $A_{IV}$ fluid

inclusion types would therefore have a close temporal relationship.

The input of a saline magmatic fluid into the San Cristobal system leads to a reinterpretation of the hydrogen and oxygen isotope data proposed by Campbell et al. (1984) and favours the model suggested by Heinrich (1990). Heinrich explained the Campbell et al. (1984) data by "minor admixture of meteoric water to a dominantly magmatic fluid, and reequilibration of the mixture with granite at 400–600 °C (at higher total fluid/rock ratio of ~ 0.15)". Indeed, the vertical trend A in Fig. 8, with a constant $\delta^{18}O$ value that is consistent with a high-temperature magmatic source but with variable $\delta D$ values extending to lower than magmatic values, can be explained by mixing of meteoric water with a dominantly magmatic fluid, rather than by equilibration of a meteoric fluid with the already cool Chumpe intrusion. An alternative explanation would be that the meteoric fluid equilibrated with host rock first, at low fluid/rock ratio as suggested by Campbell et al. (1984), and then mixed with the magmatic fluid. However, the isotopic data do not allow us to distinguish between these two mixing models. The influence of a low-temperature and low-salinity meteoric fluid is also strongly documented by the general oblique trend of primary and secondary fluid inclusion microthermometric data in a Th vs. salinity diagram (fields in Fig. 5). Uniform lead and sulphur isotope data from Moritz et al. (2001) point to a predominant magmatic source and are consistent with the model proposed by Heinrich (1990).

LA-ICP-MS results from the fluid inclusions show that the Heinrich (1990) model is probably valid for at least the two earliest vein stages where concentrations of the major mineralising metals, W, Cu and Zn, and $\delta D$ values decrease whereas $\delta^{18}O$ values remain constant (Figs. 7 and 8). Although W, Cu and Zn concentrations decrease throughout the paragenesis due to either mineral precipitation or dilution by mixing with the meteoric fluid; they do not decrease at the same rate, and the W decrease is steeper compared to the base metals (Fig. 7). These observations indicate that W was more sensitive to the deposition mechanisms than the base metal. By contrast, Na, Mn, Rb, Sr, Ba and Pb concentrations show no such decrease. These are relatively nonreactive elements (Ulrich et al., 2002). The different behaviours of the analysed elements demonstrate selective mineral precipitation (Ulrich et al., 1999). Fluid inclusions of samples located at the Mitu-Pucará contact (722-10, Fig. 2) contain significant concentrations of Pb and Zn. Potentially large quantities of base metals were then flushed out of the vein system and introduced in the carbonate replacement ore bodies. The composition of the magmatic-dominated early fluid, with thousands of ppm of W and base metals (Fig. 7), indicates that the economically interesting metals were dominantly introduced by the sporadic input of a magmatic brine. The same conclusion was deduced from porphyry-type systems (Heinrich et al., 1992; Bodnar, 1995; Ulrich et al., 1999). Whereas mixing with a fluid of meteoric origin was certainly a powerful mechanism for mineral crystallisation, it was certainly helped by interaction within the wall rocks. Indeed, higher Cu grades at the contact between rocks of the Mitu Group and the Excelsior Group may reflect pH changes in the fluid controlled by the mineralogical composition of the wall rocks. The phyllites were closer to an equilibrium state with acidic fluids than the volcanic rocks.

Homogenisation temperatures of fluid inclusions from the wolframite–quartz–pyrite stage vary over tens of degrees. Moreover, data from Campbell and Robinson-Cook (1987) indicate homogenisation temperatures that are approximately 50 °C higher than those from the $A_{II}$ fluid inclusion data of this study (Fig. 5). This temperature disparity cannot be due to the difference in elevation, and by inference in pressure, because altitude variation does not exceed 1000 m and cannot explain a difference of 50 °C. Therefore, it is preferably interpreted as temperature inversions caused by high-level flows as shown in active geothermal systems (Hedenquist et al., 1992) or the non-coexistence of the inclusions of this study and those analysed by Campbell et al. (1984). Such interpretations cannot be tested for the wolframite–quartz–pyrite stage because this stage is totally inaccessible at present due to the mining activity. However, high-level hydrothermal fluid circulations are clearly revealed by the later quartz–carbonate–barite stage.

### 7.2. Late quartz–carbonate–barite stage

Fluid inclusions in quartz III of sample 722-10, located at the Mitu-Pucará contact (Fig. 2), have

homogenisation temperatures between 253 and 323 °C and salinities ranging from 4.6 to 6.7 wt.% NaCl equiv. (Fig. 5). Nevertheless, as previously described, fluid inclusion data from this late quartz–carbonate–barite stage are inconsistent. Lisboa (2002) reported thermometric data on two samples with homogenisation temperatures between 150 and 246 °C and salinities from 2.4 to 4.5 wt.% NaCl equiv., which are both distinctly lower than values obtained on sample 722-10. Samples described by Lisboa (2002) come from the same level, but closer to the contact between the volcanic rocks of the Mitu Group and the phyllites of the Excelsior Group (Fig. 2). Due to the presence of silicified platy calcite that is interpreted as evidence of boiling (Simmons and Christenson, 1994), homogenisation temperatures must be very close to the temperature of mineral crystallisation. The variations in homogenisation temperatures and salinities may reflect a gradient originating at the Mitu-Pucará contact. A high-temperature anomaly along the Mitu-Pucará contact is consistent with field observations because the base of the Pucará Group is composed of arenites (Sallier, 2002), which have a higher permeability than surrounding rocks, and the intensively brecciated texture of the Mitu-Pucará contact was a favourable channel way for the circulation of hot fluids. A third fluid percolating through a different pathway is consistent with the geochemical data for four reasons:

- The fluids associated with the deposition of the late quartz–carbonate–barite stage are commonly enriched in $CO_2$ relative to earlier fluids (Appendix A). Indeed, most inclusions of the earlier stage are free of detectable $CO_2$ by Raman spectrometry, whereas all analysed inclusions of the late quartz–carbonate stage clearly reveal the presence of the $CO_2$ bands. It may indicate a fluid that had circulated through the Mesozoic carbonate rocks.
- LA-ICP-MS analysis of fluid inclusions of the two first stages, i.e., the early wolframite–quartz–pyrite and quartz–base metal stages, are characterised by high concentrations of base metals, whereas high Sr and Ba concentrations are typical for the late-vein stage (Fig. 7). While decreasing concentrations of W and base metals in successive fluid inclusion generations can be explained by mineral deposition, the abrupt increase of Ba and Sr concentrations in the quartz–carbonate stage can only be explained by the input of a fluid of a different origin or, at least, by a fluid that migrated along a different pathway. Such an increase in Ba and Sr concentrations was also observed in the porphyry environment by Ulrich et al. (2002), who interpreted this as a response to the destruction of Ca and Mg silicates. In the case presented here, increasing Ba and Sr concentrations may be linked to the destruction of silicates such as plagioclase and amphibole of the volcanic rocks.
- The homogenisation temperatures and salinities measured in quartz III fluid inclusions are distinctly higher than the low-temperature and low-salinity meteoric fluid deduced from data of the previous stage (Fig. 5).
- Finally, a significant influx of a fluid circulating a different pathway than the meteoric and magmatic fluids previously invoked is also suggested by highly variable $^{87}Sr/^{86}Sr$ ratios of vein barite (Moritz et al., 2001; Beuchat, 2003). On the contrary, Pb isotopic compositions of sulphides indicate that the two earlier stages are very uniform (Moritz et al., 2001; Beuchat, 2003). The $^{87}Sr/^{86}Sr$ ratios of barite appear to be correlated with the host rock, because barites hosted by the Excelsior Group are generally more radiogenic than the ones hosted by the Mitu Group (Moritz et al., 2001; Beuchat, 2003). Therefore, Pb and Sr isotopes indicate an evolution from a system with uniform isotopic composition towards an inhomogeneous system. It may be due to the change of the fluid pathway during the evolution of the hydrothermal system or the input of a third fluid.

However, both magmatic and meteoric fluid influences are still strongly suggested by the oxygen and hydrogen isotopic data. In contrast to the two first stages, the oxygen and hydrogen isotopic compositions of dickite and late-stage carbonates define an oblique trend in the $\delta D$ vs. $\delta^{18}O$ diagram (trend B in Fig. 8). This trend can be interpreted as the result of mixing of magmatic and meteoric fluids, as defined by $\delta D$ values of secondary fluid inclusions trapped in barite (Campbell et al., 1984). The change from trend A to B in Fig. 8 is interpreted to reflect the involvement of a meteoric fluid that did not equilibrate with the host rock, and probably implies a larger influx of meteoric fluid at the end of the paragenesis. Hydrogen

and oxygen isotopes do not reveal the input of an isotopically distinct third fluid as documented above. This suggests that this late fluid also had a meteoric or magmatic origin but with a different pathway. Alternatively, it may indicate a fluid that is volumetrically less important, the stable isotope signature of which is masked by the volumetrically dominant magmatic and meteoric fluids.

Cooling and slight mixing of fluids during the first two stages of mineralisation, followed by more substantial mixing during the quartz–carbonate stage, were probably the most efficient mechanisms for mineral deposition in the San Cristobal vein system. A subordinate mechanism has been $CO_2$-degassing of the fluid, at least during the quartz–carbonate stage. As mentioned before, fluid inclusions hosted in quartz III generally have higher $CO_2$ contents, which are highly variable and linked, for example, to the Mg content of the fluid (Fig. 9). The paragenetic sequence of the quartz–carbonate stage is characterised by deposition of carbonates later than the associated quartz. This is particularly obvious in sample 722-1 where crystals of rhodochrosite and ankerite have grown on the periphery of the large euhedral quartz crystals (Fig. 6). Primary fluid inclusions have higher $CO_2$ and Mg contents than secondary inclusions (Fig. 9) and it is, therefore, concluded that $CO_2$-degassing has had a local influence and may have played an important role in the deposition of the carbonate due to an increase in pH. This interpretation involving $CO_2$-degassing is in good agreement with the observation of platy calcite. Unfortunately, other carbonate cations, i.e., Ca or Fe, are generally below LOD and this assumption cannot be substantiated.

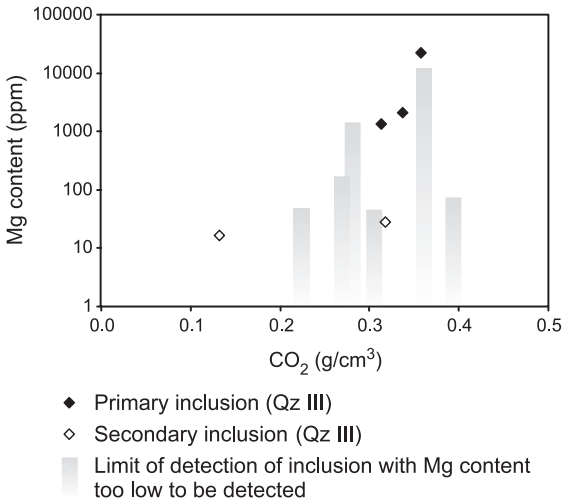


Fig. 9. Concentrations of Mg vs. $CO_2$ dissolved in fluid inclusions from quartz III. According to Rosso and Bodnar (1995), error on $CO_2$ content is equal to $\pm 0.25$ (g/cm$^3$) and error on Mg contents is shown in Appendix A.

## 8. Conclusions

The fluid inclusion and stable isotope data reveal a two-stage fluid evolution in the San Cristobal vein. Quartz of the first paragenetic stage contains two (LV) and three phase (LVH) fluid inclusions. These two fluid inclusion types are interpreted as the result of trapping of a salt-saturated fluid with a salinity between 26 and 46 wt.% NaCl equiv. $\delta$D and $\delta^{18}$O values and Pb isotope ratios overlap with the isotopic composition of the local intrusion, which strongly favours a magmatic origin for this fluid. Such high salinities are probably due to sudden decompression of the fluid exsolved by the magma (Fournier, 1999). LA-ICP-MS analyses of fluid inclusions indicate that the bulk of the economically attractive elements are provided by the fluid exsolved from the intrusion. The variation in $\delta$D values with constant $\delta^{18}$O values is interpreted to indicate mixing between a dominant magmatic fluid and a minor meteoric fluid. This mixing may have provide the depositional mechanism for the early and base metal stages. However, interaction of the fluid with the wall rocks is interpreted to have been a secondary depositional mechanism that is documented by the increase in chalcopyrite deposition at the transition between the phyllites of the Excelsior Group and the volcanic rocks of the Mitu Group.

The fluids associated with the late-stage processes have very different characteristics. The variable $\delta^{18}$O and $\delta$D values of the fluids indicate that this stage can probably still be interpreted as a magmatic–meteoric mixing event, but with a meteoric component that was no longer equilibrated with the host Chumpe intrusion. The enrichment in Ba and Sr concentrations in fluid inclusions may be attributed to the input of a third fluid along the Mitu-Pucará contact. The origin of this third fluid remains ambiguous; it could either

be a meteoric or a magmatic fluid that followed a different pathway or a fluid with a different origin. As in the earlier stages, the principal depositional mechanism is interpreted to be mixing between the different fluid components. However, platy calcite and covariation of $CO_2$ and Mg contents of the fluid inclusions suggest $CO_2$-degassing as an accessory mechanism.

## Acknowledgements

We gratefully acknowledge the Volcan Compania Minera, which provided access to underground exposures and support during fieldwork. We thank also Les Oldham and the Anglo-Peruana for advice, criticism and help during fieldwork. C. Heinrich is kindly acknowledged for the access to his laboratory at ETH Zürich. Reviews and comments by Lluis Fontboté, Ian Sampson, Andrew Campbell and Edward Ripley have greatly improved the quality of the manuscript. This study was supported by the Swiss National Science Foundation (Grant no. 2000-062000.00). **[SG]**

## Appendix A. Microthermometric and Raman spectroscopy results

| Sample | No. stage | Size (μm) | L/V | $T_E$ | $T_{mICE}$ | $T_H$ | $T_{mHALITE}$ | Salinity (wt.% equiv.) | $CO_2$ L. band | $CO_2$ U. band | $CO_2$ density (g/cm$^3$) |
|---|---|---|---|---|---|---|---|---|---|---|---|
| FPE-4a | 1 AII | 10 | – | – | – | 206 | – | 54.0[a] | – | – | – |
| FPE-4a | 2 AII | 15 | – | – | – | 206 | – | 46.1[a] | – | – | – |
| FPE-4a | 3 AII | 10 | – | – 22.2 | – | 259 | 436 | 51.7 | – | – | – |
| FPE-4a | 8 AIII | 12 | – | – 21.6 | – 2.5 | 239 | | 4.2 | / | / | / |
| FPE-4a | 9 AIII | 12 | – | – 21.6 | – 2.5 | 239 | | 4.2 | / | / | / |
| FPE-4a | 10 AIII | 10 | 1.3 | – | – 1.7 | 238 | | 2.9 | – | – | – |
| FPE-4a | 12 AIII | 12 | – | – 21.9 | – 2.6 | 156 | | 4.3 | – | – | – |
| FPE-4a | 14 AIII | 20 | – | – | – 3.1 | 219 | | 5.1 | – | – | – |
| FPE-4a | 15 AIII | 12 | 3.3 | – | – 2.8 | 218 | | 4.6 | / | / | / |
| FPE-4a | 16 AIII | 20 | – | – 29 | – 2.6 | – | | 4.3 | – | – | – |
| FPE-4a | 17 AIII | 20 | 4.9 | – 22.1 | – 2.2 | 154 | | 3.7 | 1292.0 | 1396.1 | 0.6 |
| FPE-4a | 18 AIII | 30 | 4.0 | – 21.9 | – 2.6 | 156 | | 4.3 | / | / | / |
| FPE-4a | 19 AIII | 12 | 2.5 | – | – 2.2 | 149 | | 3.7 | – | – | – |
| FPE-4a | 20 AIII | 10 | 1.8 | – | – 2.3 | 146 | | 3.9 | / | / | / |
| FPE-4a | 21 AIII | 15 | 1.8 | – | – 2.8 | 194 | | 4.6 | – | – | – |
| FPE-4a | 22 AIII | 20 | 1.9 | – | – 2.9 | 196 | | 4.8 | – | – | – |
| FPE-4a | 23 AIII | 8 | 1.9 | – 22.1 | – 1.8 | 228 | | 3.1 | – | – | – |
| FPE-4a | 24 AIII | 15 | – | – | – 2.0 | – | | 3.4 | / | / | / |
| FPE-4a | 29 AIV | 22 | – | – 20.7 | – 1.9 | 227 | | 3.2 | 1289.2 | 1392.0 | / |
| FPE-4a | 30 AIV | – | – | – 20.7 | – 1.9 | 227 | | 3.2 | – | – | – |
| FPE-4a | 31 AIV | 15 | – | – | – 1.9 | 237 | | 3.2 | 1289.4 | 1392.0 | / |
| FPE-4a | 35 AIV | 10 | – | – | – 1.7 | 229 | | 2.9 | / | / | / |
| FPE-4a | 36 AIV | 15 | – | – | – 1.7 | 228 | | 2.9 | / | / | / |
| FPE-4a | 37 AIV | 10 | – | – | – 1.7 | 228 | | 2.9 | / | / | / |
| FPE-4a | 38 AIV | 10 | – | – | – 1.7 | – | | 2.9 | – | – | – |
| FPE-4a | 39 AIV | 10 | – | – | – 1.7 | 238 | | 2.9 | / | / | / |
| FPE-4a | 40 AIV | 25 | – | – | – 2.3 | 155 | | 3.9 | 1292.2 | 1396.2 | 0.5 |
| FPE-4a | 41 AIV | 15 | – | – 27.0 | – 2.1 | 192 | | 3.5 | 1292.3 | 1395.9 | 0.4 |
| FPE-4a | 43 AIV | 15 | – | – | – 1.9 | 220 | | 3.2 | 1286.8 | 1390.8 | 0.5 |
| FPE-4a | 44 AIV | 10 | – | – | – 1.9 | 220 | | 3.2 | – | – | – |
| FPE-4a | 45 AIV | 20 | – | < – 19.0 | – 3.1 | 219 | | 5.1 | / | / | / |
| FPE-4a | 46 AIV | 50 | – | < – 19.3 | – 1.2 | 200 | | 2.1 | 1293.4 | 1396.6 | 0.2 |
| FPE-4a | 47 AIV | 50 | – | – | – 1.4 | 194 | | 2.4 | 1293.2 | 1395.8 | / |
| FPE-4a | 48 AIV | 20 | – | – | – 1.3 | 208 | | 2.2 | 1293.2 | 1397.0 | 0.5 |
| FPE-4a | 50 AIV | 40 | – | – 21.8 | – 1.4 | – | | 2.4 | 1292.3 | 1395.7 | 0.3 |

*(continued on next page)*

**Appendix A** (*continued*)

| Sample | No. stage | Size (μm) | L/V | $T_E$ | $T_{mICE}$ | $T_H$ | $T_{mHALITE}$ | Salinity (wt.% equiv.) | $CO_2$ L. band | $CO_2$ U. band | $CO_2$ density (g/cm$^3$) |
|---|---|---|---|---|---|---|---|---|---|---|---|
| FPE-4a | 51 AIV | 30 | – | – | – 1.8 | 195 | | 3.1 | 1293.8 | 1396.9 | 0.2 |
| FPE-4a | 52 AIV | 10 | – | – | – 1.6 | 200 | | 2.7 | – | – | – |
| FPE-4a | 55 AIV | 30 | – | – | – 2.4 | 215 | | 4.0 | – | – | – |
| FPE-4a | 56 AIV | 30 | – | – | – 2.4 | | | 4.0 | – | – | – |
| FPE-4a | 57 AIV | 20 | – | – 23.2 | – 2.4 | 212 | | 4.0 | 1283.5 | 1386.3 | 0.1 |
| FPE-4a | 59 AIV | 10 | – | – | – 2.5 | 211 | | 4.2 | 1283.6 | 1386.4 | / |
| 816c | 1 BI | 15 | – | – | – 2.4 | 328 | | 4.0 | 1289.4 | 1391.9 | / |
| 816c | 2 BI | 8 | – | – | – 2.3 | 328 | | 3.9 | 1289.4 | 1392.0 | / |
| 816c | 3 BI | 8 | – | – | – 2.4 | 337 | | 4.0 | / | / | / |
| DY-37 C | 1 BII | – | – | – | – 1.6 | 155 | | 2.7 | – | – | – |
| DY-37 C | 4 BII | 20 | – | – | – 1.6 | 213 | | 2.7 | 1289.2 | 1392.6 | 0.3 |
| DY-37 C | 6 BII | 15 | – | – | – 1.7 | 240 | | 2.9 | – | – | – |
| OYA-1 | 2 BII | 5 | – | – | – 2.2 | 206 | | 3.7 | – | – | – |
| OYA-1 | 3 BII | 10 | – | – | – 2.2 | 206 | | 3.7 | 1289.3 | 1392.0 | / |
| OYA-1 | 4 BII | 12 | – | – | – 2.1 | 221 | | 3.5 | / | / | / |
| OYA-1 | 5 BII | 20 | – | – | – 2.5 | 225 | | 4.2 | 1289.3 | 1392.0 | / |
| OYA-1 | 6 BII | 15 | – | – | – 2.2 | 223 | | 3.7 | – | – | – |
| 722-10 | 2 CI | 30 | 1.7 | – 23.5 | – 3.8 | 323 | | 6.2 | – | – | – |
| 722-10 | 3 CI | 20 | 1.1 | – 20.4 | – 3.6 | 310 | | 5.9 | 1282.6 | 1386.0 | 0.3 |
| 722-10 | 4 CI | 30 | 1.5 | – 22.4 | – 3.8 | 312 | | 6.2 | 1282.5 | 1385.9 | 0.3 |
| 722-10 | 5 CI | 30 | 0.9 | – 23.7 | – 3.8 | 311 | | 6.2 | 1282.3 | 1385.8 | 0.3 |
| 722-10 | 7 CI | 30 | 1.3 | – | – 4.2 | 310 | | 6.7 | – | – | – |
| 722-10 | 8 CI | 30 | – | – | – 3.6 | 302 | | 5.9 | 1282.4 | 1385.9 | 0.4 |
| 722-10 | 9 CII | 30 | 1.1 | – | – 3.8 | 263 | | 6.2 | 1283.2 | 1385.7 | / |
| 722-10 | 10 CII | 20 | 0.8 | – | – 3.7 | 266 | | 6.0 | 1283.2 | 1386.0 | / |
| 722-10 | 11 CII | 60 | 1.5 | – | – 3.3 | 275 | | 5.4 | 1283.2 | 1385.9 | / |
| 722-10 | 12 CIII | 50 | 1.0 | – 22.1 | – 3.3 | – | | 5.4 | 1283.8 | 1387.1 | 0.2 |
| 722-10 | 13 CIII | 20 | 1.8 | – | – 3.4 | 282 | | 5.6 | 1283.7 | 1387.1 | 0.3 |
| 722-10 | 14 CIII | 20 | 1.3 | – | – 3.4 | 277 | | 5.6 | – | – | – |
| 722-10 | 15 CIII | 25 | 0.7 | – 22.2 | – 3.6 | 295 | | 5.9 | 1283.3 | 1386.7 | 0.3 |
| 722-10 | 16 CIII | 40 | 1.0 | – | – 3.6 | 284 | | 5.9 | 1283.5 | 1387.0 | 0.3 |
| 722-10 | 17 CIII | 15 | 0.9 | – 19.7 | – 3.6 | 295 | | 5.9 | – | – | – |
| 722-10 | 19 CIII | 20 | 0.7 | – | – 3.8 | 250[b] | | 6.2 | 1283.2 | 1386.6 | 0.3 |
| 722-10 | 20 CIII | 35 | 0.8 | – | – 2.8 | 298 | | 4.6 | 1283.7 | 1386.7 | 0.1 |
| 722-10 | 21 CIII | 20 | 1.0 | – | – 2.9 | 319 | | 4.8 | – | – | – |
| 722-10 | 22 CIII | 25 | – | – 21.2 | – | 253 | | – | 1283.4 | 1387.1 | 0.4 |

L/V: liquid to vapour volume ratio; $T_E$: eutectic temperature; $T_{mICE:}$ temperature of the melting ice; $T_H$: LV → L homogenisation temperature; $T_{mHALITE}$: temperature of the melting of halite; /: no detected $CO_2$ band or density too low to be quantified.

[a] Salinity calculated by volume ratios of inclusion, liquid, gas and salt.

[b] Temperature of inclusion decrepitation.

## Appendix B. LA-ICP-MS results

| Na | K | Mn | Fe | Cu | Zn | As | Rb | Sr | Ba | W | Pb |
|---|---|---|---|---|---|---|---|---|---|---|---|
| 161843 | 90760 | 2169 | 37269 | 5080 | 7645 | 7690 | 611 | 176 | 1451 | 5853 | 4940 |
| 160798 | 13255 | 6074 | 34734 | 725 | 9789 | 4081 | 802 | 191 | 4426 | 11005 | 1120 |
| – | – | – | – | – | – | – | – | – | – | – | – |
| 10304 | 14354 | – | 1481 | <44 | 321 | – | – | <6 | 19 | 39 | 78 |
| 15974 | 1280 | – | 577 | <5 | 271 | – | – | 9 | 9 | 9 | 29 |
| 10888 | 1388 | – | <330 | <11 | 151 | – | – | 6 | <5 | <3 | <13 |
| 13049 | 8421 | – | 1677 | 285 | 622 | – | – | 5 | <13 | <11 | <39 |
| 17809 | 6117 | – | <932 | <25 | 275 | – | – | 23 | 23 | <7 | <37 |
| 17622 | 1788 | – | <848 | <44 | 325 | – | – | 6 | <16 | <9 | 57 |
| 15836 | 2001 | – | 953 | <7 | 454 | – | – | 6 | <5 | <4 | 39 |
| 13172 | 3773 | 638 | <5281 | 2460 | 11152 | 1153 | 162 | 27 | <112 | 106 | 242 |
| 15022 | 5461 | 437 | <2292 | 1877 | 445 | 671 | 55 | 12 | 48 | <25 | 126 |
| 12824 | 4702 | <862 | <15009 | <423 | 3053 | 2554 | <45 | <44 | <155 | <124 | <211 |
| 12837 | 6335 | 122 | 1370 | <48 | 1330 | 554 | 26 | 4 | 18 | 132 | 64 |
| 13319 | 13261 | 2190 | 9878 | 388 | 6728 | 3996 | 176 | 170 | <68 | <53 | 1110 |
| 16638 | 6029 | 602 | <3710 | <117 | 357 | 1024 | 43 | 14 | <42 | <33 | <73 |
| 15383 | 1205 | 544 | <3757 | <186 | 367 | 278 | <22 | <7 | <35 | 135 | <50 |
| 11514 | 4835 | 242 | 1239 | 271 | 171 | 344 | 42 | 24 | 26 | 9703 | 74 |
| 10933 | 3591 | – | 796 | 33 | 232 | – | – | 7 | 8 | 71 | 49 |
| 10845 | 3324 | – | 1160 | <20 | 104 | – | – | 3 | 34 | 281 | 106 |
| 11653 | 2770 | – | 670 | <30 | 639 | – | – | 17 | 321 | 123 | 57 |
| 10798 | 1639 | – | <993 | <36 | 151 | – | – | <5 | <8 | <4 | <43 |
| 11342 | 189 | – | <188 | 8 | 112 | – | – | 1 | <3 | 13 | 23 |
| 10798 | 1639 | – | <993 | <36 | 151 | – | – | <5 | <8 | <4 | <43 |
| 11157 | 671 | – | <472 | <18 | 94 | – | – | 4 | <8 | <5 | <22 |
| 11342 | 189 | – | <188 | 8 | 112 | – | – | 1 | <3 | 13 | 23 |
| 13281 | 5150 | – | <670 | <27 | <96 | – | – | <2 | 10 | <11 | <28 |
| 12372 | 4231 | – | <834 | <34 | <124 | – | – | 11 | 20 | <6 | <37 |
| 11771 | 2457 | – | <807 | <41 | <121 | – | – | 6 | <12 | <10 | <35 |
| 11771 | 2457 | – | <807 | <41 | <121 | – | – | 6 | <12 | <10 | <35 |
| 18027 | 5533 | – | 326 | 8 | 866 | – | – | 32 | 24 | 358 | 255 |
| 6890 | 2153 | – | 908 | 32 | 255 | – | – | 5 | 22 | 66 | 38 |
| 6799 | 7119 | – | <601 | <24 | 82 | – | – | 9 | <9 | 50 | <34 |
| 7704 | 2960 | – | 226 | 34 | <27 | – | – | 6 | 11 | 20 | <8 |
| 8462 | 2686 | – | <73 | 11 | 74 | – | – | 6 | 4 | 3 | 22 |
| 10899 | 3081 | – | <190 | <7 | 47 | – | – | 9 | <4 | <2 | 9 |
| 10899 | 3081 | – | <190 | <7 | 47 | – | – | 9 | <4 | <2 | 9 |
| 13678 | 5751 | 205 | <969 | <27 | 123 | 439 | 39 | 3 | 31 | 50 | 18 |
| 15591 | 7203 | 344 | 511 | <34 | 231 | 373 | 91 | 21 | 38 | 60 | 23 |
| 13586 | 5997 | 446 | <2782 | <112 | <261 | 907 | 52 | <8 | <57 | 54 | <47 |
| 14974 | 3946 | 356 | 484 | <18 | 314 | 299 | 47 | 7 | 55 | 63 | 10 |
| – | – | – | – | – | – | – | – | – | – | – | – |
| – | – | – | – | – | – | – | – | – | – | – | – |
| – | – | – | – | – | – | – | – | – | – | – | – |
| – | – | – | – | – | – | – | – | – | – | – | – |
| – | – | – | – | – | – | – | – | – | – | – | – |
| 5917 | 12368 | – | 1750 | <49 | <151 | – | – | 38 | 87 | <12 | 58 |
| 12747 | 4907 | – | <688 | 64 | 222 | – | – | <5 | <13 | <4 | 34 |
| 12747 | 4907 | – | <688 | 64 | 222 | – | – | <5 | <13 | <4 | 34 |
| 12622 | 3565 | – | <886 | <44 | 152 | – | – | 6 | 14 | <11 | <33 |
| 15014 | 3839 | – | <675 | 99 | 697 | – | – | 4 | 7 | <11 | 55 |
| 13451 | 3031 | – | <1113 | <50 | 447 | – | – | 8 | <12 | 16 | <37 |

(continued on next page)

**Appendix B** (*continued*)

| Na | K | Mn | Fe | Cu | Zn | As | Rb | Sr | Ba | W | Pb |
|---|---|---|---|---|---|---|---|---|---|---|---|
| 17516 | 7098 | 643 | 6472 | 95 | 709 | 1382 | 98 | 73 | 107 | 4 | 141 |
| 17891 | 13779 | 2339 | 1832 | 37 | 428 | 654 | 117 | 128 | 193 | < 11 | 75 |
| 19207 | 13366 | 1768 | < 1392 | 132 | 160 | 1471 | 144 | 93 | 45 | < 14 | 69 |
| 18723 | 14655 | 8144 | < 5252 | < 191 | 408 | 1635 | 140 | 118 | 192 | < 41 | < 85 |
| 24110 | 6388 | 1731 | < 4469 | 581 | 465 | 2192 | 1065 | 49 | 87 | < 59 | 172 |
| 21186 | 4991 | 261 | < 1576 | 148 | < 98 | 1157 | 56 | 36 | 83 | < 13 | 55 |
| 24219 | 4803 | 59 | < 191 | < 7 | 15 | < 7 | 79 | 20 | < 3 | < 2 | 4 |
| 23640 | 5388 | 56 | < 483 | < 33 | < 30 | < 18 | 78 | 23 | < 7 | < 6 | < 8 |
| 21293 | 2742 | 8 | < 13 | 1 | 1 | 2 | 46 | 16 | < 1 | 1 | – |
| 21293 | 938 | 65 | < 269 | < 25 | 78 | 13 | 26 | 14 | 26 | < 13 | 27 |
| 21885 | 327 | < 104 | < 1686 | < 57 | < 76 | 46 | 16 | < 4 | < 15 | < 11 | 20 |
| 21885 | 310 | < 72 | < 757 | < 30 | < 50 | < 39 | 9 | 6 | 18 | < 8 | 26 |
| 23058 | 2108 | < 61 | < 686 | < 30 | < 28 | 113 | 24 | 41 | 20 | < 8 | 18 |
| 23058 | 1428 | 11 | < 84 | < 4 | < 7 | 63 | 15 | 50 | 9 | 1 | < 2 |
| 23058 | 1761 | < 18 | < 141 | < 7 | < 12 | 65 | 18 | 52 | 15 | < 2 | < 3 |
| 24219 | 654 | < 30 | < 262 | < 14 | < 25 | 59 | 8 | 17 | < 5 | < 4 | < 6 |
| 18292 | 5067 | 62 | < 96 | 3 | 21 | 566 | 58 | 21 | 45 | < 1 | 9 |
| 15401 | 2809 | 191 | < 2141 | < 141 | < 252 | 657 | 38 | 11 | 27 | < 20 | < 36 |
| 13748 | 2819 | 73 | 7837 | 75 | 102 | 131 | 42 | 18 | 10 | < 7 | 24 |

Concentrations of each cation are indicated. <: below indicated limit of detection; –: not analysed.

## References


Bartlett, M.W., 1984. Petrology and genesis of carbonate-hosted lead–zinc–silver ores, San Cristobal district, Department of Junin, Peru. Unpublished PhD thesis, Oregon State University, Corvallis, OR, USA.

Beaty, D.W., Landis, G.P., Thompson, T.B., 1990. Carbonate-hosted sulfide deposits of the Central Colorado mineral belt: introduction, general discussion, and summary. Econ. Geol. Monogr. 7, 1–18.

Beuchat, S., 2003. Geochronological, structural, isotope and fluid inclusion constraints of the polymetallic Domo de Yauli district, Peru. PhD thesis, Terre et environnement, 41, ISBN 2-940153-40-X.

Beuchat, S., Schaltegger, U., Cosca, M., Moritz, R., Chiaradia, M., 2001. High-precision geochronology constrains on Miocene magmatic and mineralising events in the Pb–Zn–Ag–Cu Domo de Yauli district, Peru. GSA Annual Meeting, Boston, vol. A-358. In: Mineral deposits at the beginning of the 21st century, Balkema, Netherlands, pp. 381–384.

Bodnar, R.J., 1995. Fluid inclusion evidence for a magmatic source for metals in porphyry copper deposits. Short Course - Mineral. Assoc. Can. 23, 139–152.

Bodnar, R.J., Vytik, M.O., 1994. Interpretation of microthermometric data for $H_2O$–NaCl fluid inclusions. In: Vivo, B.D., Frezotti, M.L. (Eds.), Fluid Inclusions in Minerals: Methods and Applications. Virginia Polytechnic Institute, Blacksburg, pp. 117–130.

Campbell, A., Robinson-Cook, S., 1987. Infrared fluid inclusion microthermometry on coexisting wolframite and quartz. Econ. Geol. 82, 1640–1645.

Campbell, A., Rye, D., Petersen, U., 1984. A hydrogen and oxygen isotope study of the San Cristobal mine, Peru: implications of the role of water to rock ratio for the genesis of wolframite deposits. Econ. Geol. 79, 1818–1832.

Carothers, W.W., Adami, L.H., Rosenbauer, R.J., 1988. Experimental oxygen isotope fractionation between siderite–water and phosphoric acid liberated $CO_2$-siderite. Geochim. Cosmochim. Acta 52, 2445–2450.

Clayton, R.N., O'Neil, J.R., Mayeda, T.K., 1972. Oxygen isotope exchange between quartz and water. J. Geophys. Res. 77, 3057–3067.

Dalheimer, M., 1990. The Zn–Pb–Ag deposits Huaripampa and Carahuacra in the mining district of San Cristobal, Central Peru. In: Fontboté, L., Amstutz, G.C., Cardozo, M., Cedillo, E., Frutos, J. (Eds.), Stratabound Ore Deposits in the Andes. Springer-Verlag, Berlin, pp. 281–291.

Deen, J.A., Rye, R.O., Munoz, J.L., Drexler, J.W., 1994. The magmatic hydrothermal system at Julcani, Peru: evidence from fluid inclusions and hydrogen and oxygen isotopes. Econ. Geol. 89, 1924–1938.

Fournier, R.O., 1999. Hydrothermal processes related to movement of fluid from plastic into brittle rock in the magmatic–epithermal environment. Econ. Geol. 94, 1193–1212.

Gilg, H.A., Sheppard, S.M.F., 1996. Hydrogen isotope fractionation between kaolinite and water revisited. Geochim. Cosmochim. Acta 60, 529–533.

Günther, D., Heinrich, C.A., 1999. Comparison of the ablation behaviour of 266 nm Nd:YAG and 193 nm ArF excimer lasers for LA-ICP-MS analysis. J. Anal. At. Spectrom. 14, 1369–1374.

Günther, D., Audétat, A., Frischknecht, R., Heinrich, C.A., 1998. Quantitative analysis of major, minor and trace elements in fluid

inclusions using laser ablation-inductively coupled plasma-mass spectrometry (LA-ICP-MS). J. Anal. At. Spectrom. 13, 457–481.

Halter, W.E., Pettke, T., Heinrich, C.A., Rothen-Rutishauser, B., 2002. Major and trace element analysis of melt inclusions by laser-ablation ICP-MS: methods of quantification. Chem. Geol. 183, 63–86.

Hedenquist, J.W., Henley, R.W., 1985. The importance of $CO_2$ on freezing point measurements of fluid inclusions: evidence from active geothermal systems and implications for epithermal ore deposition. Econ. Geol. 80, 1379–1406.

Hedenquist, J.W., Reyes, A.G., Simmons, S.F., Taguchi, S., 1992. The thermal and geochemical structure of geothermal and epithermal systems: a framework for interpreting fluid inclusion data. Eur. J. Mineral. 4, 989–1015.

Heinrich, C.A., 1990. The chemistry of hydrothermal tin(-tungsten) ore deposition. Econ. Geol. 85, 457–481.

Heinrich, C.A., Ryan, C.G., Mernagh, T.P., Eadington, P.J., 1992. Segregation of ore metals between magmatic brine and vapor: a fluid inclusion study using PIXE microanalysis. Econ. Geol. 87, 1566–1583.

Heinrich, C.A., Pettke, T., Halter, W., Aigner-Torres, M., Audétat, A., Günther, D., Hattendorf, B., Bleiner, D., Guillong, M., Horn, I., 2003. Quantitative multi-element analysis of minerals, fluid and melt inclusions by laser-ablation inductively-coupled-plasma mass-spectrometry. Geochim. Cosmochim. Acta 67, 3473–3496.

Kobe, H.W., 1990a. Metallogenic evolution of the Yauli dome, central Peru. A summary. In: Fontboté, L., Amstutz, G.C., Cardozo, M., Cedillo, E., Frutos, J. (Eds.), Stratabound Ore Deposits in the Andes. Springer-Verlag, Berlin, pp. 267–278.

Kobe, H.W., 1990b. Stratabound sulfide occurrences in the Paleozoic of the Yauli Dome, Central Peru. A summary. In: Fontboté, L., Amstutz, G.C., Cardozo, M., Cedillo, E., Frutos, J. (Eds.), Stratabound Ore Deposits in the Andes. Springer-Verlag, Berlin, pp. 113–122.

Kusakabe, M., Robinson, B.W., 1977. Oxygen and sulfur isotope equilibria in the $BaSO_4$–$HSO_4$–$H_2O$ system from 110 to 350 °C and applications. Geochim. Cosmochim. Acta 41, 1033–1040.

Land, L.S., Dutton, S.P., 1978. Cementation of a Pennsylvanian deltaic sandstone isotopic data. J. Sediment. Petrol. 48, 1167–1176.

Landis, G.P., Rye, R.O., 1974. Geologic, fluid inclusion, and stable isotope studies of the Pasto Bueno tungsten–base metal ore deposit, northern Peru. Econ. Geol. 69, 1025–1059.

Lisboa, H., 2002. Etude le veine 722 à Zn–Pb–Ag de la mine San Cristobal (District minier de Domo de Yauli, Pérou central). Unpublished MSc thesis, University of Geneva, Switzerland.

Longerich, H.P., Jackson, S.E., Günther, D., 1996. Laser ablation inductively coupled plasma mass spectrometry transient signal data acquisition and analyte concentration calculation. J. Anal. At. Spectrom. 11, 899–904.

Megaw, P.T., Ruiz, J., Titley, S.R., 1988. High-temperature, carbonate-hosted Ag–Pb–Zn(Cu) deposits of northern Mexico. Econ. Geol. 83, 1856–1885.

Megaw, P.K.M., Barton, M.D., Falce, J.I., 1996. Carbonate-hosted lead–zinc (Ag, Cu, Au) deposits of northern Chihuahua, Mexico. In: Sangster, D.F. (Ed.), Carbonate-Hosted Lead–Zinc Deposits. SEG Special Publication, Society of Economic Geology, Littleton, Colorado, US. vol. 4, pp. 277–289.

Moritz, R., Beuchat, S., Chiaradia, M., Stucky, P., Sallier, B., Lisboa, H., 2001. Zn–Pb mantos and veins at Domo de Yauli, Central Peru: two products of one hydrothermal system with common Pb and S sources, but contrasting fluid inclusion characteristics. 6th Biennial Meeting of the SGA, Krakow, Poland. In: Mineral deposit at the beginning of the 21st century, Balkema, Netherland, pp. 173–176.

Noble, D.C., McKee, E.H., 1999. The Miocene metallogenic belt of central and northern Peru. In: Skinner, B.J. (Ed.), Geology and Ore Deposits of the Central AndesSpec. Publ. - Soc. Econ. Geol., vol. 7, pp. 155–193.

Norman, D.I., Landis, G.P., 1983. Source of mineralising components in hydrothermal ore fluid as evidenced by $^{87}Sr/^{86}Sr$ and stable isotope data from the Pasta Bueno deposit, Peru. Econ. Geol. 78, 451–465.

Pastor, J.A., 1970. The mineralization in San Cristobal mine. Unpublished MSc thesis, University of Arizona, USA.

Pettke, T., Heinrich, C.A., Ciocan, A.C., Gunther, D., 2000. Quadrupole mass spectrometry and optical emission spectroscopy: detection capabilities and representative sampling of short transient signals from laser-ablation. J. Anal. At. Spectrom. 15, 1149–1155.

Roedder, E., 1984. Fluid Inclusions. Rev. Mineral. 12, 12–26.

Rosenbaum, J., Sheppard, S.M.F., 1986. An isotopic study of siderites, dolomites and ankerites at high temperatures. Geochim. Cosmochim. Acta 50, 1147–1150.

Rosso, K.M., Bodnar, R.J., 1995. Microthermometric and Raman spectroscopic detection limits of $CO_2$ in fluid inclusions and the Raman spectroscopic characterization of $CO_2$. Geochim. Cosmochim. Acta 59, 3961–3975.

Rye, R.O., Sawkins, F.J., 1974. Fluid inclusion and stable isotope studies on the Casapalca Ag–Pb–Zn–Cu deposit, central Andes, Peru. Econ. Geol. 69, 181–205.

Sallier, B., 2002. Minéralisations stratiformes à Zn, Pb ± Ag, dans les calcaires du Pucará (Domo de Yauli, Andes du Pérou Central). Unpublished MSc thesis. University of Geneva, Switzerland, 170 pp.

Sheperd, T., Rankin, A.H., Alderton, D.H.M., 1985. A Practical Guide to Fluid Inclusion Studies. Blackie, Glasgow, UK.

Simmons, S.F., Christenson, B.W., 1994. Origins of calcite in a boiling geothermal system. Am. J. Sci. 294, 361–400.

Simmons, S.F., Arehart, G., Simpson, M.P., Mauk, J.L., 2000. Origin of massive calcite veins in the Golden Cross low-sulfidation, epithermal Au–Ag deposit, New Zealand. Econ. Geol. 95, 99–112.

Simon, K., 2001. Does $\delta D$ from fluid inclusion in quartz reflect the original hydrothermal fluid? Chem. Geol. 177, 483–495.

Smith, D.M., 1996. Sedimentary basins and the origin of intrusion-related carbonate-hosted Zn–Pb–Ag deposits. In: Sangster, D.F. (Ed.), Carbonate-hosted lead–zinc deposits. SEG Special publication, vol. 4, pp. 255–263.

Sterner, S.M., Bodnar, R.J., 1984. Synthetic fluid inclusions in natural quartz: 1. Compositional types synthesized and applications to experimental geochemistry. Geochim. Cosmochim. Acta 48, 2659–2668.

Sterner, S.M., Hall, D.L., Bodnar, R.J., 1988. Synthetic fluid inclusions: V. Solubility relations in the system NaCl–KCl–$H_2O$ under vapor saturated conditions. Geochim. Cosmochim. Acta 52, 989–1005.

Stucky, P., 2001. La veine de Pb, Zn, Cu, Ag d'Andaychagua (Domo de Yauli, Andes centrales, Pérou). Unpublished MSc thesis, University of Lausanne, Switzerland.

Taylor, H.P., 1974. The application of oxygen and hydrogen isotope studies to problems of hydrothermal alteration and ore deposition. Econ. Geol. 69, 843–883.

Titley, S.R., 1996. Characteristics of high temperature, carbonate-hosted replacement ores and some comparisons with Mississippi valley-type ores. In: Sangster, D.F. (Ed.), Carbonate-hosted lead–zinc deposits. SEG Special publication, vol. 4, pp. 244–254.

Ulrich, T., Günther, D., Heinrich, C.A., 1999. Gold concentrations of magmatic brines and the metal budget of porphyry copper deposits. Nature 399, 676–679.

Ulrich, T., Günther, D., Heinrich, C.A., 2002. The evolution of a porphyry Cu–Au deposit, based on LA-ICP-MS analysis of fluid inclusions: Bajo de la Alumbrera, Argentina. Econ. Geol. 96, 1743–1774.

Volcan annual report, 2001. Volcan compañia minera S.A.A, Lima, Peru. 167 pp.

Zhang, L.-G., Liu, J.-X., Chen, Z.-S., Zhou, H.-B., 1994. Experimental investigations of oxygen isotope fractionation in cassiterite and wolframite. Econ. Geol. 89, 150–157.